Monthly Notices
of the
ROYAL ASTRONOMICAL SOCIETY

MNRAS **471,** 3955–3973 (2017)
Advance Access publication 2017 July 15

doi:10.1093/mnras/stx1790

The SDSS-IV extended Baryon Oscillation Spectroscopic Survey: final emission line galaxy target selection

A. Raichoor,[1,2]★ J. Comparat,[3,4,5] T. Delubac,[1] J.-P. Kneib,[1,6] Ch Yèche,[2,7] K. S. Dawson,[8] W. J. Percival,[9] A. Dey,[10] D. Lang,[11] D. J. Schlegel,[7] C. Gorgoni,[1] J. Bautista,[8] J. R. Brownstein,[8] V. Mariappan,[8] H.-J. Seo,[12] J. L. Tinker,[13] A. J. Ross,[14,9] Y. Wang,[9,15] G.-B. Zhao,[9,15] J. Moustakas,[16] N. Palanque-Delabrouille,[2] E. Jullo,[6] J. A. Newmann,[17] F. Prada[4,18,19] and G. B. Zhu[20]†

Affiliations are listed at the end of the paper

Accepted 2017 July 12. Received 2017 July 7; in original form 2017 April 4

ABSTRACT

We describe the algorithm used to select the emission line galaxy (ELG) sample at $z \sim 0.85$ for the extended Baryon Oscillation Spectroscopic Survey of the Sloan Digital Sky Survey IV, using photometric data from the DECam Legacy Survey. Our selection is based on a selection box in the $g - r$ versus $r - z$ colour–colour space and a cut on the g-band magnitude, to favour galaxies in the desired redshift range with strong [O II] emission. It provides a target density of 200 deg^{-2} on the North Galactic Cap and of 240 deg^{-2} on the South Galactic Cap (SGC), where we use a larger selection box because of deeper imaging. We demonstrate that this selection passes the extended Baryon Oscillation Spectroscopic Survey requirements in terms of homogeneity. About 50 000 ELGs have been observed since the observations have started in 2016, September. These roughly match the expected redshift distribution, though the measured efficiency is slightly lower than expected. The efficiency can be increased by enlarging the redshift range and with incoming pipeline improvement. The cosmological forecast based on these first data predict $\sigma_{D_V}/D_V = 0.023$, in agreement with previous forecasts. Lastly, we present the stellar population properties of the ELG SGC sample. Once observations are completed, this sample will be suited to provide a cosmological analysis at $z \sim 0.85$, and will pave the way for the next decade of massive spectroscopic cosmological surveys, which heavily rely on ELGs. The target catalogue over the SGC will be released along with DR14.

Key words: methods: data analysis – galaxies: distances and redshifts – galaxies: photometry – galaxies: stellar content – large-scale structure of Universe – cosmology: observations.

1 INTRODUCTION

It is now well established that the star formation density of the Universe is increasing with redshift, from $z \sim 0$ to $z \sim 2$ (e.g. Lilly et al. 1996; Madau, Pozzetti & Dickinson 1998; Madau & Dickinson 2014). This implies that a typical galaxy at $z \sim 0.5$–2 will present emission lines in its spectrum (e.g. Moustakas, Kennicutt & Tremonti 2006), the most characteristic ones being the [O II] doublet (emitted at ($\lambda\lambda$3727, 3729) Å and observed in the optical) and the Hα emission line (emitted at λ6563 Å and observed in the near-infrared). These emission lines allow one to measure the spectroscopic redshift $z_{\rm spec}$ of a $z \sim 0.5$–2 galaxy within an optimized amount of observing time, without requiring a detection of the continuum at a significant level. Those two observational facts – a high density and a rapid $z_{\rm spec}$ measurement – make such star-forming galaxies the ideal tracer at $0.5 \lesssim z_{\rm spec} \lesssim 2$ for massive spectroscopic cosmological surveys, which aim to measure a large number (10^5–10^7) of $z_{\rm spec}$ within the minimum of observing time.

The WiggleZ experiment (2006–2011, Drinkwater et al. 2010) was the first survey to use such emission line galaxies (ELGs), with the observation of ∼200 000 ELGs at $z \sim 0.6$ over 800 deg^2. Future massive spectroscopic cosmological surveys heavily rely on the ELGs in the $0.5 \lesssim z \lesssim 2$ range: PFS[1] (2019, Sugai et al. 2012;

★ E-mail: anand.raichoor@epfl.ch
† Hubble fellow.

[1] Prime Focus Spectrograph: http://sumire.ipmu.jp/en/2652/.

Takada et al. 2014) will target 4 million ELGs at $0.8 < z < 2.4$ over 1400 deg^2, DESI[2] (2019, DESI Collaboration et al. 2016a,b) will target 28 million ELGs at $0.6 < z < 1.6$ over 14 000 deg^2, 4MOST[3] (2021, de Jong et al. 2014) will target 7 million ELGs at $0.7 < z < 1.1$ over 5000 deg^2 and *Euclid* (2020, Laureijs et al. 2011) will obtain 50 million redshifts from ELGs at $0.8 < z < 1.8$ over 15 000 deg^2, based on their Hα emission line.

The extended Baryon Oscillation Spectroscopic Survey (eBOSS; 2014–2020, Dawson et al. 2016) programme of the fourth generation of the Sloan Digital Sky Survey (SDSS; York et al. 2000) experiment will pave the way for those next generations surveys, as it will also use ELGs as tracers at $z \sim 0.8$. Since its beginning, the SDSS experiment has been constraining the nature of dark energy through the measurement of the baryon acoustic oscillations (BAOs) signal in the two-point clustering of galaxies at different redshifts. SDSS I-II (Abazajian et al. 2009) measured at $z = 0.35$ the distance–redshift relation with a 5 per cent precision (Eisenstein et al. 2005) through the observation of 45 000 luminous red galaxies (LRGs; Eisenstein et al. 2001), making the first BAO detection along with the 2dF Galaxy Redshift Survey (Colless et al. 2003; Cole et al. 2005). The Baryon Oscillation Spectroscopic Survey (BOSS; 2008–2014, Dawson et al. 2013) from the SDSS-III (Eisenstein et al. 2011) observed 1.5 million galaxies and 160 000 quasars, which led to 1 per cent to 2 per cent precision measurements of the cosmological distance scale for redshifts $z < 0.6$ and $z = 2.5$ (Delubac et al. 2015; Ross et al. 2017).

eBOSS is one of three surveys from the SDSS-IV experiment (Blanton et al. 2017): it will use 1 million objects divided in four different tracers to expand the volume covered by BOSS focusing on the redshift range $0.6 < z < 2.2$. The four eBOSS tracers are LRGs at $z \sim 0.7$ (Prakash et al. 2016), ELGs at $z \sim 0.8$, 'CORE' quasars at $0.9 < z < 3.54$ (Myers et al. 2015) supplemented by variability-selected ($2.1 < z < 3.5$) quasars (Palanque-Delabrouille et al. 2016); the quasars at $z < 2.2$ are used as direct probes of large-scale structure, and those at $2.1 < z < 3.5$ are used to trace Lyman α absorbers along their line of sight. Regarding the ELGs, 300 plates are dedicated to the observation of 255 000 ELG targets with the BOSS spectrograph (Smee et al. 2013), in order to produce a 2 per cent precision distance estimate (Zhao et al. 2016). The Fig. 1 illustrates how the eBOSS programmes combine with the previous SDSS BAO programmes, thus probing the Universe over more than 70 per cent of its history. The top panel shows the observed tracers, colour-coded by programmes, while the bottom panel displays the Universe rate of expansion as a function of redshift, along with the redshift range used for each tracer for the BAO measurement

We present in this paper the final target selection for the eBOSS/ELG programme, for which observations started in 2016, September. The target selection is a key step in such cosmological experiments, as it will define the data sample used for the cosmological analysis. It has to fulfil requirements with respect to the subsequent cosmological analysis (number of redshifts, area, homogeneity), but also with respect to the observational constraints (availability of sufficiently wide and deep imaging survey, reliable $z_{\rm spec}$ measurement with the instrument in the available observing time). According to previous experience with BOSS and cosmological forecast, the ELG target selection should fulfil the following criteria (Dawson et al. 2016): (1) a surface density $>170\,{\rm deg}^{-2}$; (2) an absolute variation in expected density <15 per cent with respect

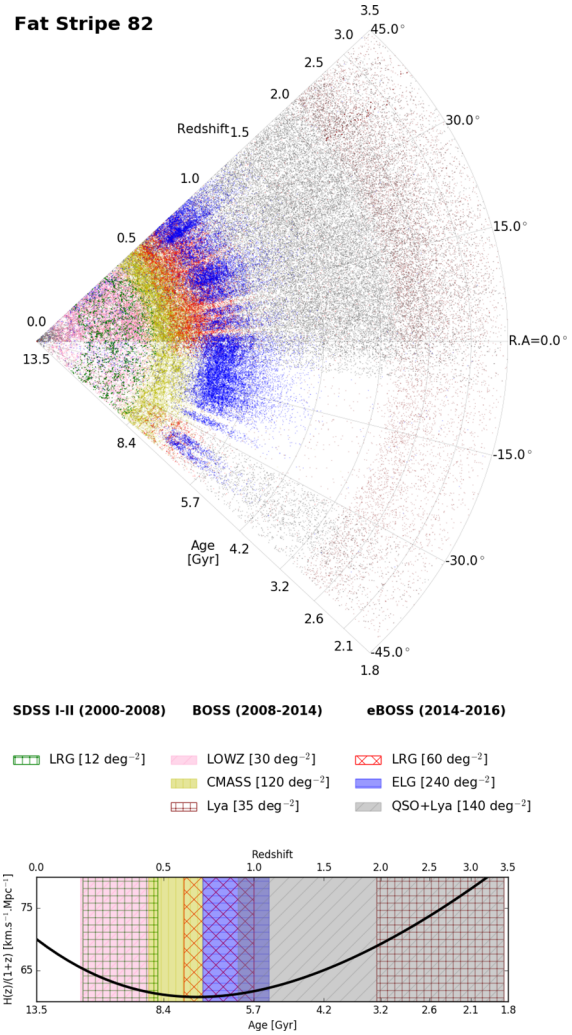

Figure 1. Compilation of the SDSS BAO surveys in the Fat Stripe 82 (see Section 2.1). The LRG programme from SDSS I-II is in green. The LOWZ, CMASS and Lyman α programmes from BOSS are in pink, yellow and brown, respectively. The LRG, ELG, QSO+Lyman α programmes from eBOSS are in red, blue and grey, respectively; for eBOSS, we report the data observed between 2014 and 2016. For BOSS and eBOSS, the density in the $0° < RA < 45°$ is higher than in $-45° < RA < 0°$, because the included range in declination is higher ($-5° <$ Dec. $< 5°$ versus $-2° <$ Dec. $< 2°$). *Top panel*: sector view of observed targets. *Bottom panel*: Universe rate of expansion as a function of redshift, along with the redshift range used for each tracer for the BAO measurement.

to imaging depth, Galactic extinction and stellar density; (3) an absolute variation in expected density <15 per cent with respect to the estimated uncertainties in the imaging zero-point; (4) reliable $z_{\rm spec}$ measurements, i.e. with a precision better than $300\,{\rm km\,s}^{-1}$; (5) an ELG sample used for cosmology at $z \sim 0.85$ $>190\,000$, i.e. >74 per cent of the observed targets with a reliable $z_{\rm spec}$ measurement with $0.7 < z_{\rm spec} < 1.1$; (6) <1 per cent of this sample with a catastrophic $z_{\rm spec}$ measurement (redshift error exceeding $1000\,{\rm km\,s}^{-1}$).

Though the SDSS has more than a decade experience in target selection for cosmological surveys, the ELG target selection required a significant testing phase before the start of the programme, because it is the very first time this tracer is used in the SDSS and because the targeted redshift is challenging for a 1–1.5 h observation with the BOSS spectrograph. In a preliminary work, Comparat

[2] Dark Energy Spectroscopic Instrument: http://desi.lbl.gov/.
[3] 4-m Multi-Object Spectroscopic Telescope: https://www.4most.eu/.

et al. (2013) studied the feasibility of an ELG programme with the BOSS spectrograph, concluding positively. They demonstrated that a sufficiently high density of ELGs could be selected from optical photometry and that their $z_{\rm spec}$ could be efficiently measured with the BOSS spectrograph. Comparat et al. (2016a) led a detailed study of the $z_{\rm spec}$ measurement of ELGs with the BOSS spectrograph, using pilot surveys of different target selections. They demonstrated the reliability of the $z_{\rm spec}$ measurement, and developed a posteriori flags that ensure the rate of catastrophic measurement is <1 per cent. Then, Raichoor et al. (2016) presented a possible target selection based on the SDSS imaging, with a target density of 180 deg^{-2}: thanks to public data and dedicated test plates observed with the BOSS spectrograph, they showed that ∼70 per cent of this selection has $0.6 < z_{\rm spec} < 1.0$, with an expected catastrophic rate of ∼1 per cent. Delubac et al. (2017) demonstrated that this selection passed the density homogeneity requirements.

However, the recent advent of the DECam Legacy Survey[4] (DECaLS; Dey et al., in preparation) provided an opportunity to design a further ELG target selection, which presented the noteworthy advantage of being at higher redshift than the one presented in Raichoor et al. (2016) and Delubac et al. (2017). This one, based on the DECaLS imaging, was chosen by the eBOSS team, and is the one we present hereafter. We present in Section 2 the DECam observations and DECaLS photometric catalogues, which are used to define the target selection. Section 3 details the target selection algorithm. We demonstrate in Section 4 that the selection passes the homogeneity requirements. Section 5 presents the first months of observations, which have started in 2016 September, the redshift distribution and the cosmological forecast based on these observed plates. Those first observations are then used to present in Section 6 the mean photometric, spectroscopic and structural properties of the ELG sample. We conclude in Section 7.

We consider a standard cosmology with $H_0 = 70\,{\rm km\,s^{-1}\,Mpc^{-1}}$, $\Omega_{\rm m} = 0.30$, and $\Omega_\Lambda = 0.70$, except in Section 5.5, where the *Planck* cosmology (Planck Collaboration XIII 2016) is assumed for the cosmological forecast. All magnitudes are in the AB system (Oke & Gunn 1983) and have been corrected for Galactic extinction using the maps of Schlegel, Finkbeiner & Davis (1998).

2 IMAGING AND PHOTOMETRY

The eBOSS/ELG target selection is based on the DECaLS data, processed independently by us, but using the same pipeline and software. Thorough tests have been conducted to design the eBOSS/ELG target selection. Raichoor et al. (2016) and Delubac et al. (2017) have presented a target selection based on the SDSS imaging, which passed the eBOSS requirements. Though the SDSS imaging has the great advantage of being highly homogeneous and understood, its shallowness limits the target selection performance, decreasing the median redshift and the efficiency. The deeper imaging of the DECaLS survey allows one to design a target selection with higher redshift and higher efficiency, even with current observations not reaching yet the nominal depth.

The DECaLS (co-PIs: A. Dey and D.J. Schlegel) is an on-going imaging survey covering 6700 deg^2 of the extragalactic sky that lies in the region $-20^\circ <$ Dec. $< +30^\circ$ to depths of $g = 24.7$, $r = 23.9$ and $z = 23.0$ mag (5σ point-source). In addition, the DECaLS programme also processes any public DECam observations in the DESI footprint, the largest component being the Dark Energy Survey (DES). The DECaLS data and processing pipeline are public, with a release every six months. DECaLS will be used as the main imaging for the DESI target selection, which will observe ∼35 million targets, of which ∼28 million will be ELGs (DESI Collaboration et al. 2016a).

[4] http://legacysurvey.org/

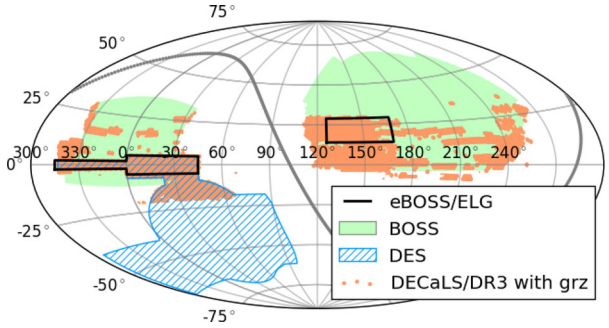

Figure 2. Survey footprints: eBOSS/ELG footprint (black lines; SGC is on the left, NGC is on the right), SDSS/BOSS footprint (light green shaded regions), DES footprint (blue hatched), and DECaLS/DR3 regions with *grz* imaging (orange dots).

2.1 ELG footprint over the SGC and the NGC

The eBOSS/ELG footprint is divided in two regions (see Fig. 2):

(i) ∼620 deg^2 over the Fat Stripe 82 in the South Galactic Cap (SGC), covered by DES observations; the boundaries are: ($317^\circ < RA < 360^\circ$ and $-2^\circ <$ Dec. $< 2^\circ$) or ($0^\circ < RA < 45^\circ$ and $-5^\circ <$ Dec. $< 5^\circ$);

(ii) ∼600 deg^2 over the North Galactic Cap (NGC), covered by DECaLS observations; the boundaries are: $126^\circ < RA < 168^\circ$ and $14^\circ <$ Dec. $< 34^\circ$.

The exact footprint over the NGC may be updated when the plates position and targets fibre assignment are set (tiling), as the DECaLS observations in this region are not yet complete (see Section 2.2 below).

2.2 Imaging observations

The eBOSS/ELG target selection is based on the imaging included in the Data Release 3 (DR3), the third public data release of images and catalogues for the DECaLS. DECaLS/DR3 includes DECaLS *grz*-band observations (co-PIs: A. Dey and D.J. Schlegel; NOAO Proposal # 2014B-0404) from 2014 August through 2016 March, and DECam data from a range of non-DECaLS surveys, including observations that were conducted from 2012 September to 2016 March. For the currently tiled part of the eBOSS/ELG NGC footprint, we also included 28 DECaLS exposures from 2016 April 08–10. Fig. 2 displays the 4200 deg^2 of DECaLS/DR3 observed in all three *grz* bands.

All observations included in DECaLS/DR3 are made with the DECam camera (Flaugher et al. 2015) mounted at the prime focus of the Victor M. Blanco 4-m telescope on Cerro Tololo near La Serena, Chile. The DECam camera has a 3 deg^2 field of view covered by 62 2k×4k CCDs for imaging, with a resolution of 0.262 arcsec pixel^{-1}.

DECaLS observations follow a three-pass tiling strategy, with nominal exposure times of $[t_g, t_r, t_z] = [70, 50, 100]$ s; those nominal exposure times are dynamically adjusted during the observations in order to optimize the observing efficiency (see Burleigh et al., in preparation for details). DECaLS observations over

Table 1. Imaging properties over the eBOSS/ELG footprint. We report the median values. The depth is 5σ point-source depth. The NGC numbers are for the DECaLS/DR3 imaging covering our footprint in the *grz* band, described in Section 2.2.

Region	Area (deg^2)	Observing programme	Filter	nexp	texp (s)	Seeing (arcsec)	Depth (mag)
SGC	∼620	DES	*g*	4	360	1.6	24.7
			r	3	270	1.2	24.5
			z	3	270	1.1	23.3
NGC	∼600	DECaLS	*g*	2	140	1.4	24.0
			r	2	100	1.3	23.6
			z	1	120	1.2	22.6

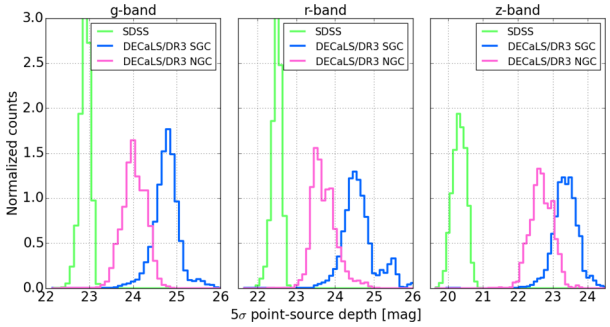

Figure 3. DECam imaging depths over our ELG footprint (SGC in cyan, NGC in pink). We report the SDSS (green) to illustrate the improvement brought by DECaLS.

the eBOSS/ELG NGC footprint are still on-going: the part of eBOSS/ELG NGC footprint not covered with *grz* bands in DR3 (∼200 deg^2, see Fig. 2) will be observed in the first semester of 2017; we will include all DECaLS/post-DR3 observations available over the footprint before the final tiling. Note that those data will be processed with the very same DR3 pipeline, which has been used already for the data presented in this paper.

The DES[5] (2013–2018; PI: J. Frieman; NOAO Proposal # 2012B-0001) is an on-going *grizY*-imaging survey over 5000 deg^2, down to $i \sim 24.1$ mag (10σ, extended source). At the end of the 5 yr of observations, DES will have observed each region with 10 individual exposures, with typical exposure times of 90 s for the *grz* bands.

Imaging properties over the eBOSS/ELG footprint are summarized in Table 1, and the imaging depths over this footprint are displayed in Fig. 3. Over the NGC, the DECam imaging is about 1 mag deeper than the SDSS imaging in the *g* and *r* bands, and about 2 mag deeper in the *z* band. Over the SGC, the DECam imaging is about 2 mag deeper than the SDSS imaging in the *g* and *r* bands and about 3 mag deeper in the *z* band; when compared to the DECam NGC imaging, the DECam SGC imaging is about 0.8 mag deeper.

2.3 Data processing and photometry

We processed the images with the DECaLS/DR3 pipeline,[6] which is based on the TRACTOR[7] (Lang et al., in preparation). Apart from source detection that uses stacked images, all measurements are based on individual exposures. Astrometric calibration is tied to Pan-Starrs1 measurements (Kaiser et al. 2010), as is the photometric calibration, with the use of a colour correction term to transform the PS1 magnitudes into a DECam-based system. Each source is modelled with an analytic profile (point-source, exponential with fixed parameters, exponential, de Vaucouleurs or composite) and a model image is generated for each exposure. Increasingly more complex profiles are allowed for sources detected with higher signal-to-noise ratio. The source properties (position, shape, flux) are measured through a likelihood optimization (χ^2 minimization) of the set of model images covering the considered region. For our purpose, this approach has the advantage to provide accurate colours, based on the same profile for all bands and accounting for the point spread function (PSF).

We processed the data independently of the DECaLS team for the two following reasons. First, because the target catalogues were required for the tiling before the public release of DECaLS/DR3. Secondly, as the DECaLS imaging over our ELG NGC footprint is not yet finished, we will later on process any new DECaLS imaging in our ELG NGC footprint, thus using the very same pipeline version. A posteriori comparison with the publicly released DECaLS/DR3 catalogues has shown that source detections and flux measurements in regions processing the same imaging data set were virtually similar, resulting in identical target catalogues.

3 TARGET SELECTION ALGORITHM

The eBOSS/ELG target selection is based on three criteria: (i) clean photometry, using catalogue flags, and masking bright star/object neighbourhoods; (ii) favouring [O II] emitters, through a cut in the *g*-band magnitude – this band, the bluer available for our photometry, correlates with the [O II] flux ($F_{[\mathrm{O\,II}]} \propto 10^{-0.35\times g}$; see Comparat et al. 2016b), as it favours galaxies with high flux in the ultraviolet rest frame ($\lambda_{\mathrm{r.-f.}} \sim 2400$–$3000$ Å at $0.7 < z_{\mathrm{spec}} < 1.1$), and hence with the presence of a significant population of massive, new-born stars; (iii) selecting galaxies in the desired redshift range, through a box cut in the $g - r$ versus $r - z$ colour–colour diagram (*grz* diagram, hereafter).

The corresponding cuts, detailed in Table 2, have been fine-tuned with thorough tests, using various photometric and spectroscopic public catalogues and dedicated observations with the BOSS spectrographs. In particular, the $g \lesssim 22.8$ cut is set by the constraint to significantly detect the [O II] line in the spectrum within ∼1 h of BOSS observation (while the $21.8 \lesssim g$ cut is mainly set to reject low-redshift contamination).

A coding error in the target selection scripts[8] translates to an additional rejection mask for the ∼400 deg^2 already tiled in the NGC (chunk `eboss23`, see Section 5.1). The effect of this mask is to reject ∼15 per cent of the targets in the NGC, which explains

[5] http://www.darkenergysurvey.org

[6] For a more detailed description, please see: http://legacysurvey.org/dr3/description/.

[7] https://github.com/dstndstn/tractor

[8] At the step of rejecting areas with shallow depths in the NGC, we read the depth brick images ($0.^\circ25 \times 0.^\circ25$) to obtain the depth at a target position; we took the (*x*,*y*) position instead of the (*y*,*x*) position. This results for ∼15 per cent of the targets in reading the depth at a position without imaging coverage because of the CCD gaps, hence a rejection. The main consequence is that objects that should have been observed are not observed. The ∼0.5 per cent of observed objects, which should have not been observed, can be *a posteriori* rejected when making the cosmological analysis, using minimum `depth_ivar` values of 62.79, 30.05 and 11.00 for the *g*, *r* and *z* bands, respectively. This error is fully reproducible, and hence can be accounted for in the clustering analysis, especially at the step of random generation.

Table 2. eBOSS/ELG target selection over the SGC and the NGC footprints. The reported densities are computed with the plate covered areas (i.e. not accounting for the masked regions). The DECaLS catalogue quantities `BRICK_PRIMARY`, `decam_anymask` and `tycho2inblob` are described here: http://legacysurvey.org/dr3/catalogs/.

Criterion	eBOSS/ELG SGC [240 deg^{-2}]	eBOSS/ELG NGC [200 deg^{-2}]
Clean photometry	SDSS bright object mask[a] and 0 mag $< V <$ 11.5 mag Tycho2 stars mask `BRICK_PRIMARY` and `decam_anymask[grz]` $= 0$ and `tycho2inblob==False` Custom mask[b] [chunk `eboss23` only]	
[O II] emitters	$21.825 < g < 22.825$	$21.825 < g < 22.9$
Redshift range	$-0.068 \times (r-z) + 0.457 < g - r < 0.112 \times (r-z) + 0.773$ $0.218 \times (g-r) + 0.571 < r - z < -0.555 \times (g-r) + 1.901$	$-0.068 \times (r-z) + 0.457 < g - r < 0.112 \times (r-z) + 0.773$ $0.637 \times (g-r) + 0.399 < r - z < -0.555 \times (g-r) + 1.901$

Notes. [a]http://data.sdss3.org/sas/dr10/boss/lss/reject_mask/.
[b]This custom mask is used because of a bug in the target selection scripts, and is relevant for the chunk `eboss23` only.

why we select objects slightly fainter in the g band in the NGC to reach our target density of 200 deg^{-2}.

In order to profit from the DES imaging depth over the eBOSS/ELG SGC footprint, our selection has a higher density in the SGC than in the NGC. The deeper, hence less scattered, DES photometry allows us to enlarge our selection box in the grz space towards blue $r - z$ colour, with keeping a low contamination level from lower redshift galaxies.

Fig. 4 illustrates the cuts in the grz space. This figure is for illustration purpose only; it allows one to visually identify the expected redshift and [O II] loci over the eBOSS/ELG SGC and NGC areas, showing the impact of the imaging depth on the grz band. We consider the CFHTLS/*W*4 region ($\sim$20 deg^2 at RA $= 333^\circ$ and Dec. $= 2^\circ$; Gwyn 2012), which is covered by DES deep observations. The redshift information is taken from the CFHTLS photometric redshifts (Ilbert et al. 2006; Coupon et al. 2009) and the [O II] flux is measured from the VIPERS survey spectra (Guzzo et al. 2014; Scodeggio et al. 2016). The displayed photometry is the original DECaLS/DR3 photometry, degraded to the depths over the eBOSS/ELG SGC and NGC footprints. To do so, for each of the grz band, we add in quadrature random noise to the original photometry in order to reproduce the magnitude error–magnitude relation (see section 3.1 of Raichoor et al. 2016). Also, as our selection is based on a cut on the g-band magnitude, we randomly remove objects to reproduce the incompleteness in source detection for faint sources in the typical NGC/SGC data. The eBOSS/ELG NGC area has an imaging depth $\sim$0.8 mag shallower than the eBOSS/ELG SGC area: this implies a larger scatter on the photometry and, as a consequence, less well-defined loci in terms of redshift. Restricting to a smaller colour–colour box in the grz diagram for the eBOSS/ELG selection over the NGC prevents our target selection to be contaminated by $z < 0.7$ objects: as those objects have a higher density than the $0.7 < z < 1.1$ objects, the scattering due to shallow photometry would imply more $z < 0.7$ objects entering our selection than $0.7 < z < 1.1$ objects exiting our selection.

4 SYSTEMATICS

To ensure that our clustering analysis and cosmological measurements will be limited by statistical uncertainties, the target density should pass a list of homogeneity requirements, mainly derived from knowledge of the BOSS survey. As stated in Section 1, the target density should have a <15 per cent variation with respect to imaging PSF and depth, Galactic extinction, and stellar density; and it also should have a <15 per cent variation with respect to the estimated uncertainties in the imaging zero-point.

In this section, we present a thorough analysis on the density variation over the footprint, similar to that presented in Ross et al. (2011), Myers et al. (2015), Prakash et al. (2016) and Delubac et al. (2017) for other samples, to which we refer the reader for the details.

4.1 Dependency over the observational parameters

As a first step, we use the whole DECaLS/DR3 footprint to construct a map of the potential sources of systematic error in target selection due to variations in stellar density, Galactic extinction, grz PSF and depth: those maps are displayed on the left column panels in Figs 5–7. We divide our maps into equal-area pixels of $\sim$0.05 deg^2 (corresponding to HEALPIX[9] `nside` $= 256$), and compute n, the target density in each pixel, for both SGC and NGC selections. Then, for each footprint (SGC and NGC), we measure in each pixel the normalized average number density ($n/\overline{n}$, $\overline{n}$ being the mean density over the footprint), and look at its variation with each of these systematics.

The solid lines in the lower panels in the right column of Figs 5–7 show those dependences. The selections over the SGC and the NGC have very similar behaviour, which is expected given that they are based on very similar cuts. These curves are computed for the full DECaLS/DR3 footprint: the upper panels in the right column plots of Figs 5–7 display the cumulative histograms of the systematics over the eBOSS/ELG SGC and NGC footprints. The histograms thus indicate the relevant systematics range for each selection. Cumulative histograms over the full DECaLS/DR3 footprint are also reported in black. For instance, the g-band depth over the eBOSS/ELG SGC and the NGC footprints are distributed differently: 90 per cent of the SGC footprint has a g-band imaging deeper than 24.4 mag, whereas the corresponding depth for the NGC footprint is 23.7 mag. Overall, the target density variations over the SGC and NGC footprints are satisfactory. For each observational parameter, the variation in target density is always smaller than 12 per cent over the range including the 10 per cent to 90 per cent of the cumulative histograms; the only exception being for the z-band depth for the NGC selection, where the variation in the target density is $\sim$20 per cent.

Some of the dependences can be explained as follows. The target density decreases with increasing stellar density; it has been shown in Ross et al. (2011) and Delubac et al. (2017) that this can be understood as resulting from the low stellar contamination of our selections plus the fact that each star masks a small area of the sky, preventing the selection of targets in that area. However, we

[9] http://healpix.jpl.nasa.gov/

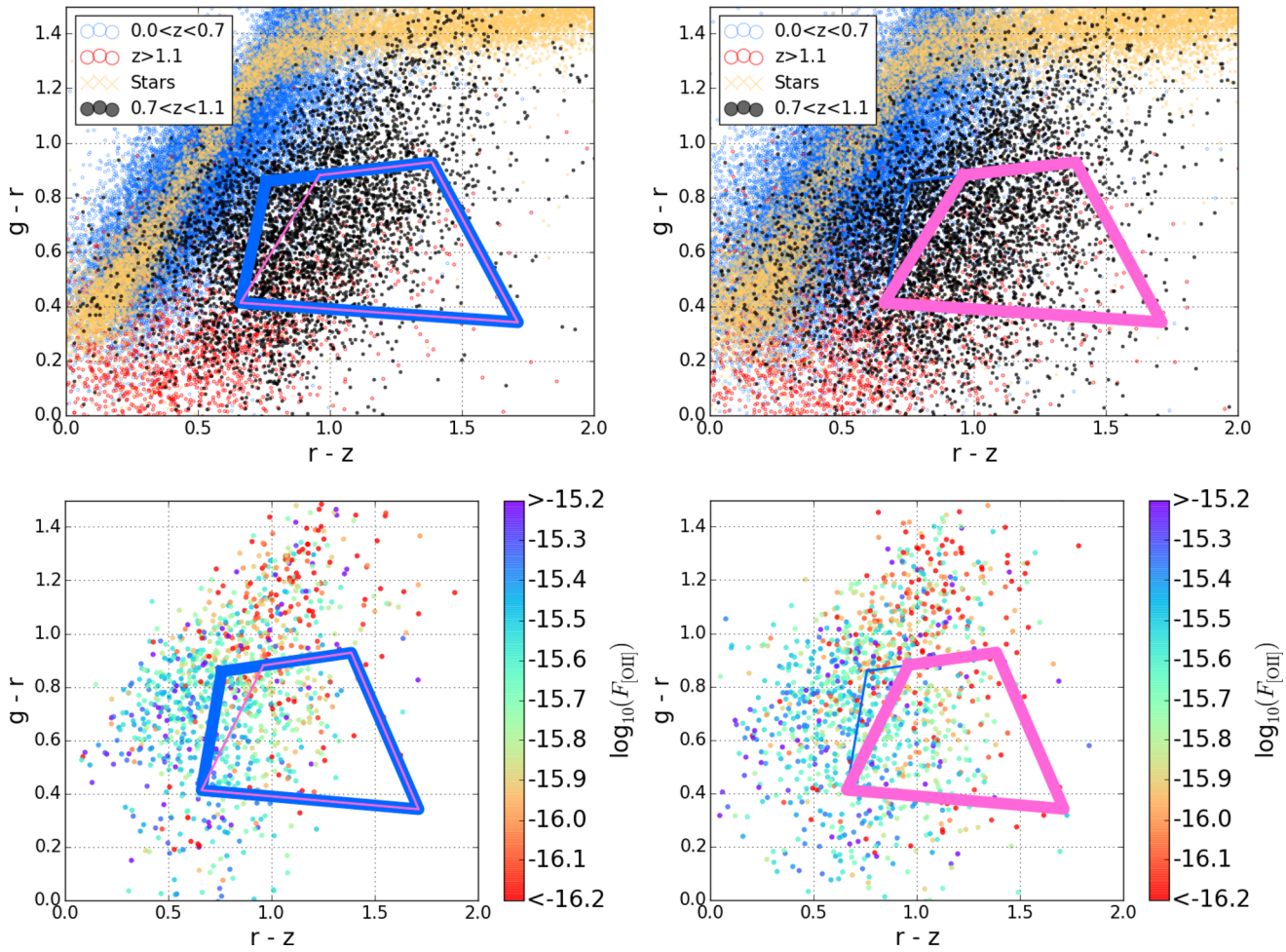

Figure 4. eBOSS/ELG selection in the *grz* colour space for the CFHTLS/*W*4 field. Our *grz* selection over the eBOSS/ELG SGC area (NGC area, respectively) is displayed as the cyan (pink, respectively) box. We display objects after applying the 'clean photometry' and '[O II] emitters' cuts (see Table 2). *Left:* photometry from DECaLS/DR3 over the CFHTLS/*W*4 (DES observations), degraded down to DECaLS/DR3 depths over the eBOSS/ELG SGC footprint. *Right*: photometry from DECaLS/DR3 over the CFHTLS/*W*4 (DES observations), degraded down to DECaLS/DR3 depths over the eBOSS/ELG NGC footprint. *Top panels*: photometric redshifts are taken from the CFHTLS survey: stars are displayed as beige crosses, $0 < z_{\rm phot} < 0.7$ objects as blue circles, $0.7 < z_{\rm phot} < 1.1$ objects as black dots and $1.1 < z_{\rm phot}$ objects as red circles. *Bottom panels*: we only display objects in common with the VIPERS survey with $0.6 < z_{\rm spec} < 1.1$; [O II] fluxes are measured from the VIPERS survey spectra.

underline that the stellar density over the ELG footprint has limited impact as the density is generally low; for instance, 90 per cent of the ELG footprint have $n_{{\rm stars}_g} < 2000\,{\rm deg}^2$. The target density also decreases with increasing Galactic extinction; this is expected because of the luminosity function shape, as the faintest objects in g band, removed from our selection by a high Galactic extinction value are overwhelmingly more numerous than the brightest ones which enter our selection. Additionally, there is also a correlation between the stellar density and the Galactic extinction. The target density has a clear dependence on the g-band depth, with an increase for deeper imaging. This can be explained by the fact that our selections are based on a g-band magnitude cut and that deep imaging will provide more detected objects.

4.2 Modelling the systematic effects

We then simultaneously model the effect of those systematics using a multivariate regression, as in Delubac et al. (2017). We use a quadratic dependence as a function of the Galactic extinction, the g- and z-band PSF, the r- and z-band depth, which exhibit explicit non-linear behaviour and a linear dependence as a function of all other systematics.

Once we have modelled how the target selection depends on the systematics, we can compute $n^{\rm pred}$, the predicted density of the selection in the absence of shot noise and cosmic variance given the value of the systematics. As shown in Delubac et al. (2017), it is then possible to reduce the effect of those systematics on the target density by applying a correction with a weighting defined as $w_p = 1 + \frac{\overline{n} - n^{\rm pred}}{n}$. Figs 5–7 show that applying such a correction to the pixel densities actually reduces the systematic effects (dashed lines); the fluctuations of the normalized average number density $n/\overline{n}$ are now consistent with zero given the uncertainties computed as the root mean square in the bin. Note that once the spectroscopic ELG observations are complete that weights will be re-computed using the ELG cosmological sample.

We present in Fig. 8 the maps of these predicted densities $n_{\rm pred}$ (top and middle panels), along with their distribution (bottom panels); note this quantity is different from the measured pixel densities n. In the histogram panel, we emphasize two regions corresponding to a ± 7.5 per cent fluctuation around 234 and 190 ${\rm deg}^{-2}$. The

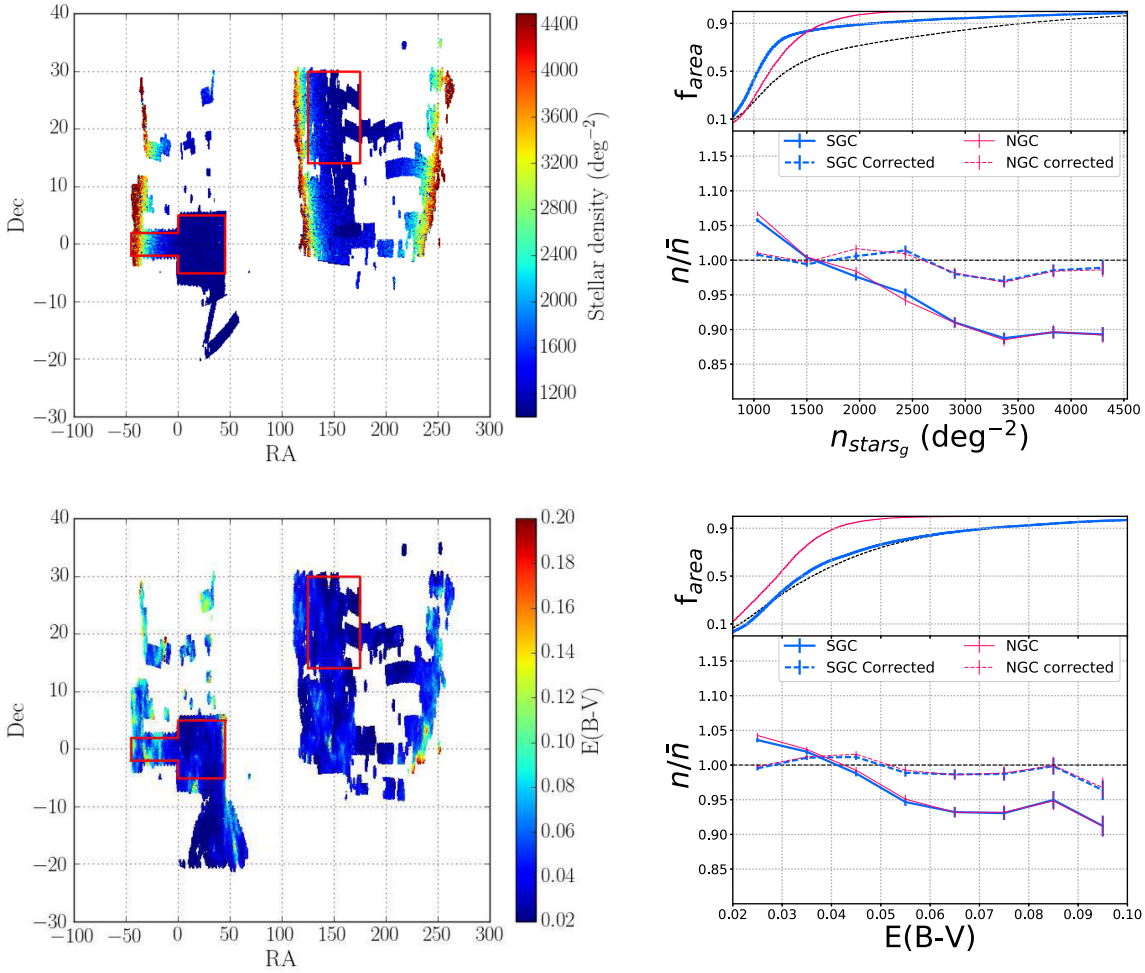

Figure 5. Target selection dependency on the stellar density (*top*) and the Galactic extinction (*bottom*). *Left*: maps of the observational parameters. *Right*: normalized average number density ($n/\overline{n}$) as a function of each observational parameter. Cyan curves are for the eBOSS/ELG SGC selection and pink curves are for the eBOSS/ELG NGC selection. In each panel on the right, the top curve shows the fractional area of the survey which has a value of the parameter lower than or equal to the x-axis value; the black dashed line stands for the full DECaLS/DR3 footprint. In the bottom panels, the solid lines correspond to the uncorrected density fluctuations, while the dashed curves represent the fluctuations remaining after applying the weights defined in the section 4.2.

choice of the central values is somewhat arbitrary, but they broadly correspond to the maximum of the distribution of the two selections, i.e. they are close to maximizing the surface of the footprint passing the homogeneity requirements. With these central values, 84.5 per cent deg^2 of the SGC footprint and 72.2 per cent deg^2 of the NGC footprint pass the homogeneity requirement.

4.3 Zero-point fluctuations

We test the zero-point requirement for each photometric band individually, following an approach similar to the one presented in Dawson et al. (2016), Myers et al. (2015) and Prakash et al. (2016). We add ± 0.01 mag to each photometric band used and then re-run the target selection algorithm to estimate $\delta N_{0.01} = \frac{|\Delta N|}{N}$, the change in target density due to this ± 0.01 mag shift. In the g, r and z bands, we find for $\delta N_{0.01}$ values of 3.6 per cent, 4.3 per cent and 2.9 per cent, respectively, for the SGC, and of 3.4 per cent, 4.0 per cent and 2.9 per cent, respectively, for the NGC.

We quantify the fraction of the footprint area which passes the ± 7.5 per cent uniformity requirement as in Dawson et al. (2016). Let it be σ_{zp}, the expected rms error in the photometric calibration of the considered band. We use the σ_{zp} error estimates of Finkbeiner et al. (2016) for the SDSS bands (summarized in Table 3); these have been estimated for the SDSS with Pan-Starrs1, which is the very same survey used by DECaLS for its zero-point calibration. For a given band, uniformity with 15 per cent peak-to-peak amplitude occurs in regions where the zero-point is in error by less than $\pm 0.01 \times \frac{7.5}{\delta N_{0.01}}$. Using the σ_{zp} error estimates of Finkbeiner et al. (2016) and assuming Gaussian errors for the zero-points, this happens for >97.9 per cent of the footprint in all bands (see Table 3). The selections are robust against variation of the imaging zero-points.

Another way to consider this is that the expected rms variation in target density due to shifts of the imaging zero-point is $\frac{\delta N_{0.01}}{0.01} \times \sigma_{zp}$ (Myers et al. 2015; Prakash et al. 2016). Assuming Gaussian errors for the zero-points, 95 per cent of our footprint lies within a $\pm 2\sigma_{zp}$ variation from the expected zero-point of any given photometric band, meaning that 95 per cent of our footprint has a variation in target number density lower than $4 \times \sigma_{zp} \times \frac{\delta N_{0.01}}{0.01}$. The resulting fluctuations for each photometric band are given in Table 3. Both selections have fluctuations of 9 per cent to 13 per cent, below the

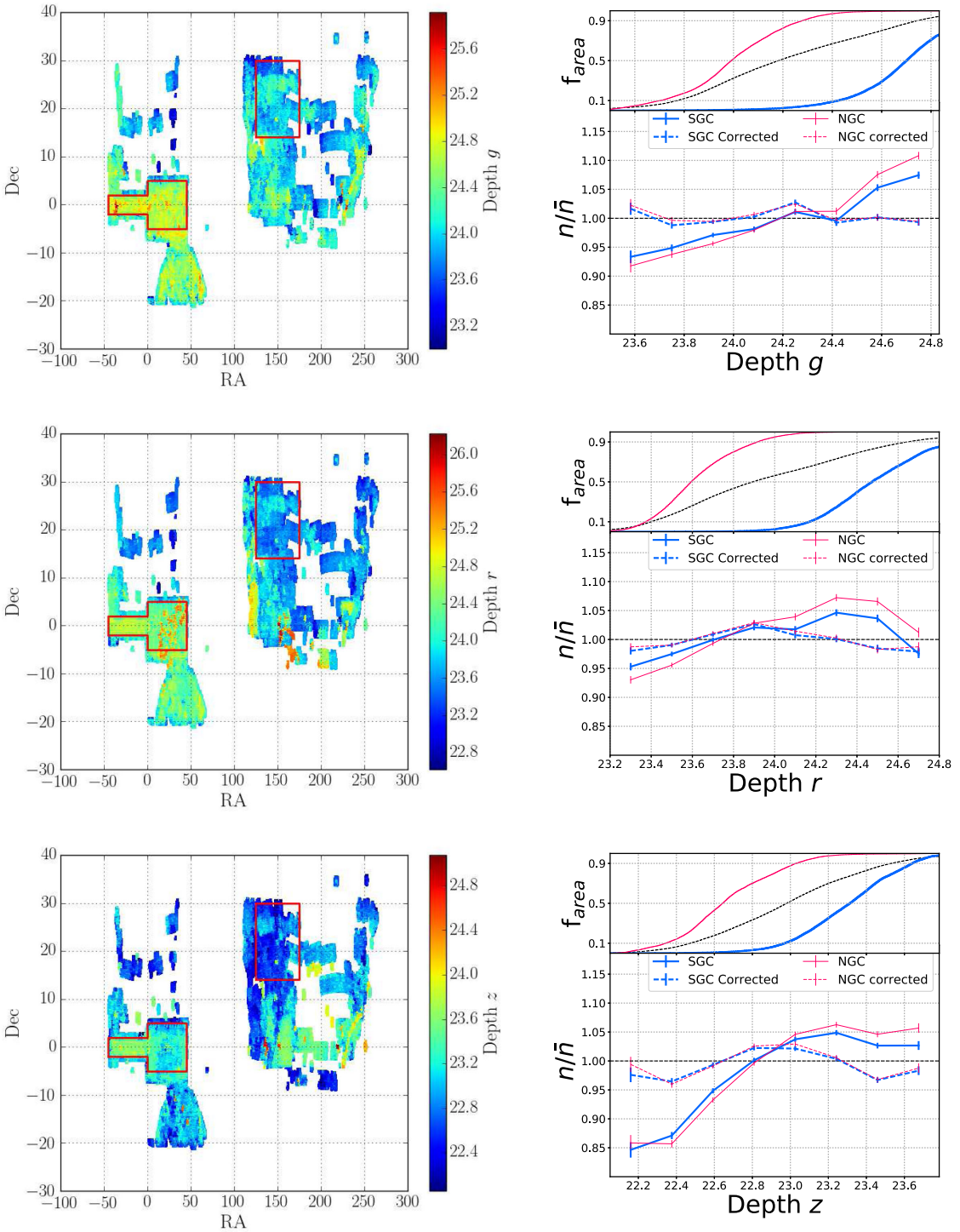

Figure 6. As Fig. 5 but for the DECaLS imaging depth in the g, r, and z bands (from top to bottom).

15 per cent requirements, thus confirming that the selections pass the zero-point requirement.

4.4 Catalogue public release

The target catalogue over the SGC footprint will be publicly released in mid-2017, as a Value-Added Catalog from the SDSS DR14 release (http://www.sdss.org/dr14/data_access/vac/, Abolfathi et al. 2017). It will contain the DECaLS `brickname`, the (RA, Dec.) coordinates, the *grz*-band magnitudes and magnitude errors, along with the systematic weights fitted in Section 4.2.

5 FIRST MONTHS OF OBSERVATIONS

We describe here preliminary results from the first months of observations (57656 $\leq$ `MJD` $\leq$ 57787). The general procedure for the

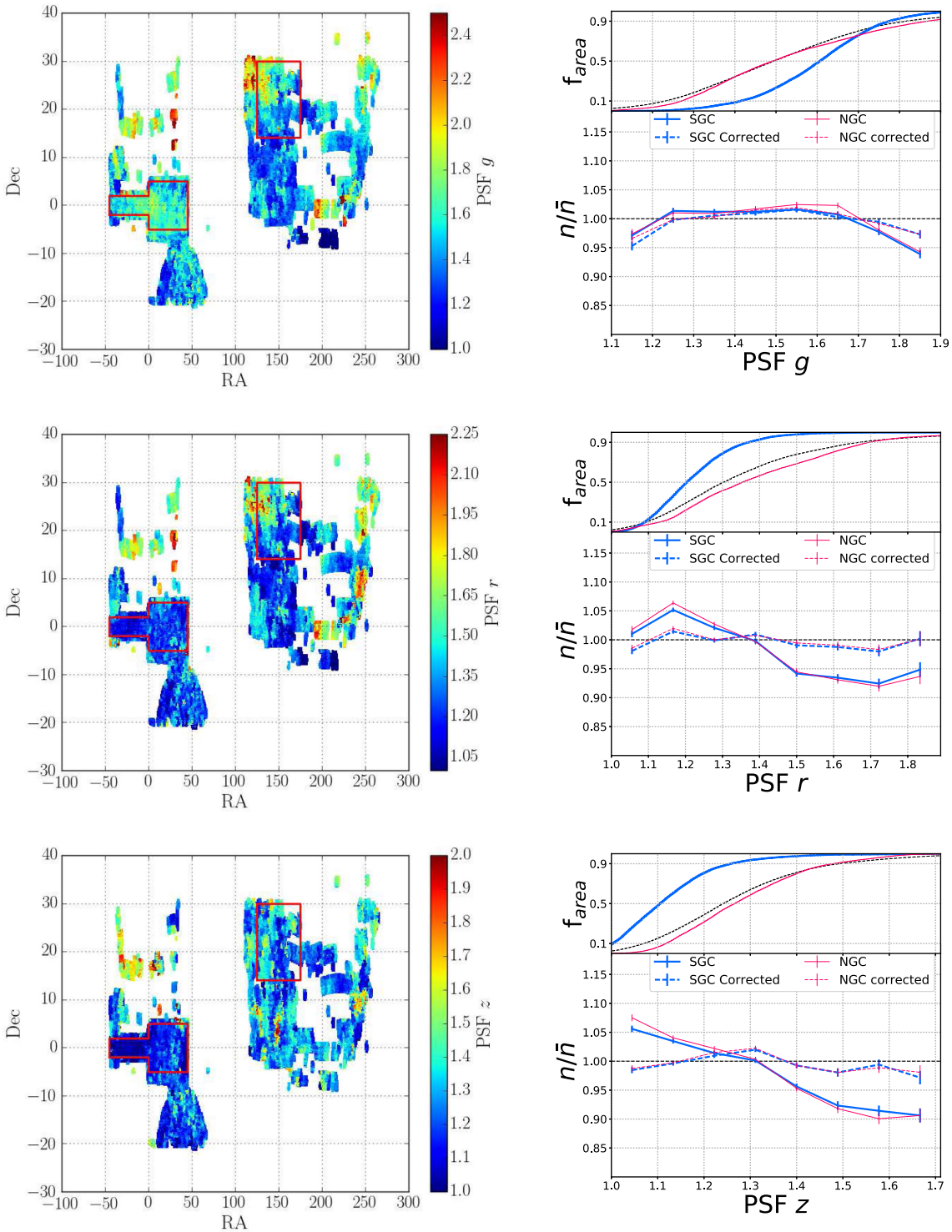

Figure 7. As Fig. 5 but for the DECaLS imaging PSF in the g, r, and z bands (from top to bottom).

spectroscopic observations is described in details in the eBOSS overview paper (Dawson et al. 2016): we only report here a brief summary, and items specific to the ELG programme. The spectroscopic observations are conducted with the BOSS spectrograph at the 2.5-m aperture Sloan Foundation Telescope at Apache Point Observatory in New Mexico (Gunn et al. 2006). From the first data, we are able to determine the actual efficiency, which we define as the percentage of observed ELG targets having a reliable $z_{\rm spec}$ estimation (equation 1) and $0.7 < z_{\rm spec} < 1.1$.

5.1 Tiling, plate design and exposure time

Once the target catalogue is built from the photometric catalogue, one has to define the plate tiling and which targets are assigned

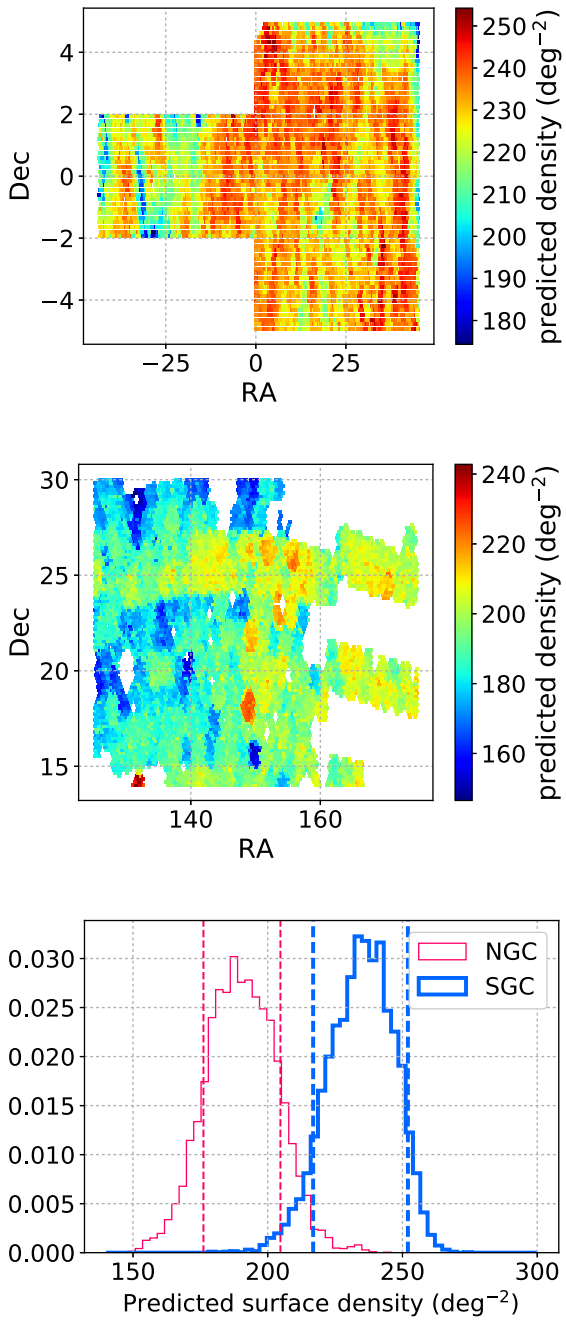

Figure 8. Predicted pixel densities for both selections. *Top panel*: map of the predicted densities for the SGC. *Middle panel*: map of the predicted densities for the NGC. *Bottom panel*: histogram of the predicted densities; the dashed vertical lines mark a ±7.5 per cent fluctuation around 234 and 190 deg^{-2}, broadly corresponding to the maximum of the distribution of the two selections.

a fibre. For the SGC, the tiling has been designed in two *chunks*, 46 plates at $317^\circ < RA < 360.0$ (`eboss21`) and 121 plates at $0^\circ < RA < 45^\circ$ (`eboss22`). For the moment, only ∼400 deg^2 of the NGC footprint is tiled (`eboss23`, 87 plates): the rest of the footprint will be tiled in the second semester of 2017, based on the DECaLS imaging available at that time. Fig. 9 shows the plate tiling, along with the tiling completeness, defined as the fraction of targets that were assigned a fibre. For a typical ELG observed plate, the 1000 fibres available are used as follows: ∼100 fibres are used for calibration targets (as for all eBOSS plates), ∼50 fibres are dedicated for the Time Domain Spectroscopic Survey (Morganson et al. 2015; Dawson et al. 2016) programme and ∼850 fibres are dedicated to ELG targets. For both footprints, the tiling completeness is ∼98 per cent in plate overlapping regions and ∼87 per cent where there is only one plate covering. The overall tiling efficiency is 95.1 per cent in the SGC and 91.5 per cent in the NGC.

During the plate design, the assigned targets celestial coordinates are converted to the coordinate system of the telescope focal plane. The ELG targets are centred on the focal plane at a position (`LAMBDA_EFF`) corresponding to the focus of 7500 Å light: this choice optimizes the signal, as it broadly corresponds to the location of the [O II] emission at redshift 1.

The exposure time is dynamically adapted every 15 min at the telescope to obtain a homogeneous sample with a redshift success rate as constant as possible. After each exposure, the median-squared signal-to-noise ratio in the red camera (`rSN`^{2}; masked from the sky OH lines) is measured: the observers then decide whether or not the observed plate requires more exposure to reach the nominal `rSN`^{2}. During the first month of operations (57656 ≤ `MJD` ≤ 57711, 19 plates), the plates were exposed longer, so that those data can be used to optimize the exposure time. To sample at most the explored parameters space, we re-reduce the data for some plates, including only a subsample of the individual exposures. Fig. 10 illustrates the obtained results. From this plot it is clear that, when the `rSN`^{2} is low, the pipeline is unable to provide a reliable redshift at an efficient rate. For example, the efficiency – as defined in Section 5 – is only ∼50 per cent when a plate is exposed to a depth of `rSN`$^2 = 10$. In addition, the efficiency of the pipeline in producing reliable redshifts begins to approach a plateau in the range of $20 <$ `rSN`$^2 < 30$. For example, the efficiency only increases from 63 per cent at `rSN`$^2 = 20$ to 70 per cent at `rSN`$^2 = 30$. Given that `rSN`^{2} scales linearly with exposure time, more tracers are classified by investing the time towards a new plate than to increase the signal by this amount. Accounting for those measurements and for the expected available time to run the ELG programme, we established a threshold of `rSN`$^2 > 22$ for all ELG exposures, which broadly corresponds to an average of 4.5 15 min exposures per plate.

5.2 $z_{\rm spec}$ measurement and reliability flags

The results presented in this paper used version `v5_10_2` of the IDLSPEC2D data reduction pipeline to extract and flux-calibrate the ELG spectra. For each observed target, the one-dimensional extracted, observed spectrum is compared to a set of star, quasar and galaxy templates, and the object type and redshift $z_{\rm spec}$ are estimated through a χ^2-minimization procedure. The galaxy templates are constructed through a linear combination of a four distinct eigenspectra derived from principal component analysis (PCA). The templates used in this analysis are those used for redshift estimation in BOSS. The derivation of PCA eigenspectra and the exact prescription for redshift fitting with these templates is described in Bolton et al. (2012).

This `v5_10_2` version of the eBOSS pipeline includes several improvements over version `v5_9_0` that was used to compute the spectra in DR13 (SDSS Collaboration et al. 2016), including direct corrections for differential atmospheric refraction as documented in Jensen et al. (2016) and a new methodology for co-addition of multiple exposures as documented in Hutchinson et al. (2016). A nearly identical version of the pipeline will be used for all data taken through 2016 May 11 to be released as DR14. Although these

Table 3. Impact of fluctuations in imaging zero-points on the number densities of the selections. The second column is the expected rms error in the photometric calibration (σ_{zp}). The third and sixth columns are the change in target density due to a ±0.01 mag shift in the zero-point ($\delta N_{0.01} = \frac{|\Delta N|}{N}$). The fourth and seventh columns are the fraction of the footprint passing the ±7.5 per cent uniformity requirement. The fifth and eighth columns are the fluctuations in density over 95 per cent of the footprint.

Band	σ_{zp}	SGC selection			NGC selection		
		$\delta N_{0.01}$	Fraction passing ±7.5 per cent	Fluctuation over 95 per cent of the area	$\delta N_{0.01}$	Fraction passing ±7.5 per cent	Fluctuation over 95 per cent of the area
	(mmag)	(per cent)	(per cent)	(per cent)	(per cent)	(per cent)	(per cent)
g	9	3.6	97.9	13.0	3.4	98.6	12.2
r	7	4.3	98.7	12.0	4.0	99.3	11.2
z	8	2.9	99.9	9.3	2.9	99.9	9.3

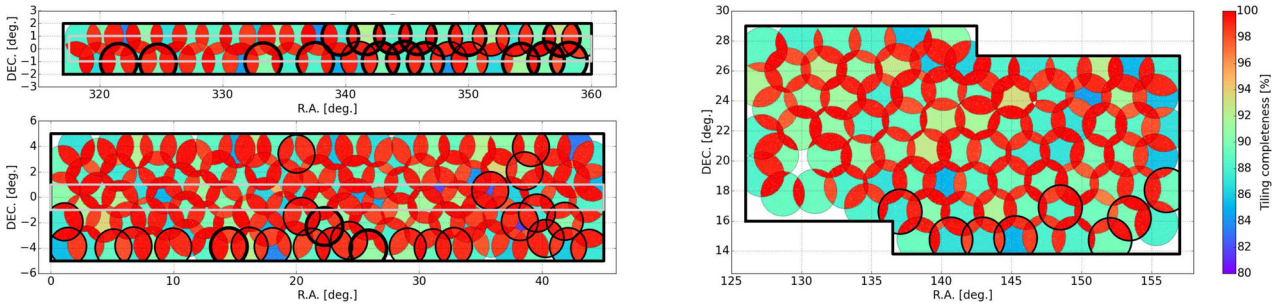

Figure 9. Tiling completeness for the ELG plates. The full SGC tiling is presented in the top left (chunk `eboss21`, 46 plates) and bottom left (chunk `eboss22`, 121 plates) panels. The currently tiled NGC area is presented in the right-hand panel (chunk `eboss23`, 87 plates). The percentage of photometric targets being assigned a fibre is colour-coded for each sector defined by the plate overlaps. Observed plates are circled in black; plates observed between 57656 ≤ MJD ≤ 57711 with exposure times longer than nominal are circled in thick black; the grey rectangle in the left-hand panels shows the CS82 imaging survey footprint.

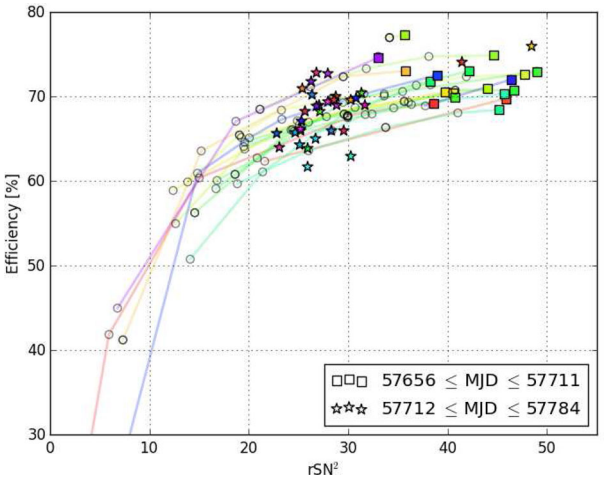

Figure 10. Efficiency (as defined in Section 5) as a function of $\mathtt{rSN}^2$ for the ELG plates observed in the SGC with longer exposure time (57656 ≤ MJD ≤ 57711). For each plate, the final reduction with all observed individual exposures is displayed as a filled square. A given plate can have several reductions with different exposure subsets: in this case, those are displayed as empty circles and linked by a thin line of a given colour to the final reduction square. Plates observed after having set the nominal $\mathtt{rSN}^2$ (57712 ≤ MJD ≤ 57749) are displayed as stars.

ELG spectra will not be in that public sample, they will be publicly released in 2019 with a new version of the data reduction pipeline that is expected to have a better sky subtraction algorithm.

Because the templates were optimized for passive galaxies that dominated the BOSS selection, the current pipeline is not optimized for characterizing ELG spectra. We further compute *a posteriori* flags (zQ, zCont) to characterize the physical nature of the spectral template and thus assess the reliability of the spectroscopic redshift estimations. Those flags, quantifying the signal-to-noise ratio (S/N) in emission lines (zQ flag) and in the continuum (zCont flag), are introduced in Comparat et al. (2016a).

For the zQ flag, we use the same definition as in Comparat et al. (2016a), which quantifies the number and significance of the measured emission lines; for instance, $zQ = 4$ corresponds to two lines detected with S/N > 5, $zQ = 2$ corresponds to one line detected with S/N > 5 and $zQ = 1$ corresponds to one line detected with 3 < S/N < 5.

For the continuum flag zCont, we consider the spectrum in $3500 < \lambda[\text{Å}]/(1+z_{spec}) < 3800$ and apply a 15 Å [O II] mask from $3726 - 15 < \lambda[\text{Å}]/(1+z_{spec}) < 3728 + 15$. We set $zCont = 0$ (1 and 2.5, respectively) if the ratio of the median flux observed to the standard deviation of the flux is ≤3 (in]3, 8] and ≥8, respectively); in this way, the selection criterion of reliable redshifts with the flags remains similar to the one defined in the equation (2) of Comparat et al. (2016a):

$$\text{zQ} \geq 2 \text{ or } (\text{zQ} \geq 1 \text{ and } \text{zCont} > 0) \text{ or } (\text{zQ} \geq 0 \text{ and } \text{zCont} \geq 2.5). \quad (1)$$

The REDMONSTER method (Hutchinson et al. 2016), which currently provides eBOSS LRG redshift, will eventually be ported to ELG to improve the redshift efficiency, thanks to the use of more physically meaningful spectral templates.

5.3 Error on z_{spec} and catastrophic z_{spec}

As mentioned in the introduction, the ELG selection must fulfil two criteria with respect to the z_{spec} measurement precision.

The first one is $\sigma_v < 300\,\mathrm{km\,s^{-1}}$, which can be expressed with σ_z, the error on the $z_{\rm spec}$ measurement as $\frac{\sigma_z}{1+z} = \frac{\sigma_v}{c} < 10^{-3}$ (see Dawson et al. 2016). Our observed ELGs with a reliable $z_{\rm spec}$ estimation (equation 1) and $0.7 < z_{\rm spec} < 1.1$ have on average $log_{10}(\sigma_z) = -4.00 \pm 0.24$, with only ∼10 ELGs over >30 000 having $\sigma_z > 10^{-3}$. Hence, the criterion on $\sigma_v < 300\,\mathrm{km\,s^{-1}}$ is passed by our ELG target selection. Note that, as analysed in details in Comparat et al. (2016a), the pipeline σ_z tightly anticorrelates with the [O II] flux.

The second criterion is that <1 per cent of the ELGs with a reliable $z_{\rm spec}$ estimation (equation 1) and $0.7 < z_{\rm spec} < 1.1$ have a catastrophic $z_{\rm spec}$ measurement. Based on visual inspection, Comparat et al. (2016a) have demonstrated that the (zQ, zCont) flag selection of equation (1) results in ∼1 per cent catastrophic $z_{\rm spec}$ for a sample similar to our selection (similar target selection, $g < 22.8$, $0.7 < z_{\rm spec} < 1.1$). Furthermore, the visual inspection of two additional plates (9199 and 9210) provides an estimation of the catastrophic assignment rate of 1.4 per cent, thus in broad agreement with the analysis of Comparat et al. (2016a), made on observations previous to the official ELG programme.

5.4 Redshift distribution and selection efficiency

Fig. 11 and Tables 4 and 5 detail the redshift distribution $n(z)$ when considering only observed targets with a reliable $z_{\rm spec}$ (equation 1). We compute the surface densities (Table 4) correcting for the tiling incompleteness and using the plate covered areas (i.e. not accounting for the masked regions). We normalize the total target density to the mean density over chunks `eboss21` and `eboss22` for the SGC, and over chunk `eboss23` for the NGC. The volume densities (Table 5) are computed from the surface densities reported in Table 4, assuming a 95 per cent tiling completeness, and our standard cosmology ($H_0 = 70\,\mathrm{km\,s^{-1}\,Mpc^{-1}}$, $\Omega_{\rm m} = 0.30$ and $\Omega_\Lambda = 0.70$).

For the SGC, we split the sample between plates observed with a longer exposure time ($57656 \leq$ `MJD` ≤ 57711, 19 plates) and plates observed with a nominal exposure time ($57712 \leq$ `MJD` ≤ 57749, 32 plates). The former have better statistics than the latter, as less galaxies are rejected because of unreliable $z_{\rm spec}$ measurement. The sample with longer exposure times has 71.9 per cent of the observed targets with a reliable $z_{\rm spec}$ with $0.7 < z_{\rm spec} < 1.1$, versus 68.0 per cent for the sample with nominal exposure times. The $57656 \leq$ `MJD` ≤ 57711 sample has 19.3 per cent of unreliable $z_{\rm spec}$, whereas the $57712 \leq$ `MJD` ≤ 57749 sample has 15.2 per cent unreliable $z_{\rm spec}$.

When comparing the $n(z)$ between the SGC and the NGC, we see that the two selections have overall a similar redshift distribution shape (median $z_{\rm spec}$ of 0.84) and are efficient at removing stars and $z_{\rm spec} < 0.6$ objects. However, the NGC sample has a lower efficiency, with 63.1 per cent of the observed targets with a reliable $z_{\rm spec}$ with $0.7 < z_{\rm spec} < 1.1$.

Though those efficiencies are lower than the goal of 74 per cent, there are several ways to increase them: (1) consider $0.6 < z_{\rm spec} < 1.1$ instead of $0.7 < z_{\rm spec} < 1.1$: this adds ∼5 per cent to the efficiency, without changing the percentage of catastrophic $z_{\rm spec}$; (2) refine the redshift quality flags zQ and zCont: visual inspection has shown that about ∼50 per cent of the rejected objects with $0.7 < z_{\rm spec} < 1.1$ have a reliable $z_{\rm spec}$ (Comparat et al. 2016a): including these objects in the final sample would add∼4 per cent to the efficiency; (3) improve the pipeline reduction (e.g. using REDMONSTER, improving the sky subtraction), as we currently reject 15–20 per cent of the observations because of the $z_{\rm spec}$ reliability criterion. It is difficult to quantify the anticipated improvement in the efficiency brought by this pipeline improvement. However, those three items should at least be able to bring the efficiency close to 75 per cent for the SGC and close to 70 per cent for the NGC. Given that the cosmological forecast analysis made with the current efficiencies (see Section 5.5) provides predicted BAO measurements with a precision close to the one computed with the nominal efficiency of 74 per cent, we conclude that this final efficiencies for the ELG programme should be sufficient to reach the aimed precision on the BAO measurement.

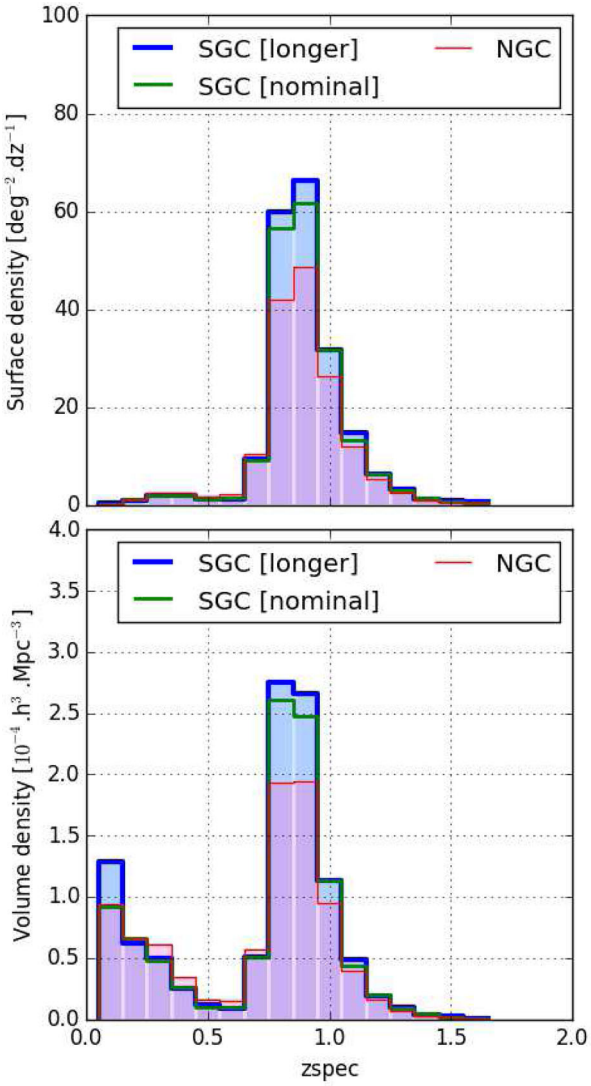

Figure 11. ELG $n(z)$ for the ELG plates observed between $57656 \leq$ `MJD` ≤ 57787. We consider only objects with a reliable $z_{\rm spec}$, i.e. passing the equation (1). For the SGC, we split the sample between the plates observed with $57656 \leq$ `MJD` ≤ 57711 (longer exposure times), and the plates observed with $57712 \leq$ `MJD` ≤ 57749 (nominal, shorter exposure times). *Top panel*: distribution per surface density. *Bottom panel*: distribution per volume density.

5.5 Cosmological forecast

We compare here the cosmological forecast using the redshift distributions presented in Section 5.4, with that presented in Zhao et al. (2016). Zhao et al. (2016) present a complete cosmological

Table 4. Measured surface density for the ELG plates (in deg^{-2}). The $z_{\rm spec}$ is considered as reliable if it passes the equation (1). The densities are corrected for tiling incompleteness. Densities for within the $0.7 < z_{\rm spec} < 1.1$ are reported in bold, and their summed density is reported in the penultimate line of the table, along with the efficiency in the last line. For the SGC, we split the sample between the plates observed with $57656 \leq$ MJD ≤ 57711 (longer exposure times), and the plates observed with $57712 \leq$ MJD ≤ 57749 (nominal, shorter exposure times).

Redshift	SGC longer	SGC nominal	NGC
Unreliable	36.4	46.4	43.2
Star	1.2	1.2	1.4
$0.0 < z < 0.1$	0.3	0.2	0.3
$0.1 < z < 0.2$	1.1	1.1	1.1
$0.2 < z < 0.3$	2.1	2.0	2.6
$0.3 < z < 0.4$	1.9	1.9	2.6
$0.4 < z < 0.5$	1.3	1.1	1.7
$0.5 < z < 0.6$	1.3	1.4	2.2
$0.6 < z < 0.7$	9.3	9.2	10.3
$0.7 < z < 0.8$	**59.8**	**56.6**	**42.0**
$0.8 < z < 0.9$	**66.2**	**61.6**	**48.5**
$0.9 < z < 1.0$	**31.6**	**31.6**	**26.3**
$1.0 < z < 1.1$	**14.9**	**13.4**	**12.0**
$1.1 < z < 1.2$	6.3	6.4	5.4
$1.2 < z < 1.3$	3.2	2.9	2.5
$1.3 < z < 1.4$	1.3	1.5	0.9
$1.4 < z < 1.5$	0.9	0.7	0.4
$1.5 < z < 10.0$	0.7	0.6	0.5
Total targets	240.0	240.0	204.0
Total tracers	**172.6**	**163.3**	**128.8**
Efficiency	**71.9 per cent**	**68.0 per cent**	**63.1 per cent**

Table 5. Measured volume densities for the ELG plates (in $10^{-4}\,h^3\,{\rm Mpc}^{-3}$). The densities correspond to the densities per area reported in Table 4, assuming a 95 per cent tiling completeness, and our standard cosmology ($H_0 = 70\,{\rm km\,s^{-1}\,Mpc^{-1}}$, $\Omega_{\rm m} = 0.30$ and $\Omega_\Lambda = 0.70$). Densities within $0.7 < z_{\rm spec} < 1.1$ are reported in bold. For the SGC, we split the sample between the plates observed with $57656 \leq$ MJD ≤ 57711 (longer exposure times), and the plates observed with $57712 \leq$ MJD ≤ 57749 (nominal, shorter exposure times).

Redshift	SGC longer	SGC nominal	NGC
$0.0 < z < 0.1$	1.281	0.915	0.939
$0.1 < z < 0.2$	0.625	0.663	0.662
$0.2 < z < 0.3$	0.493	0.478	0.611
$0.3 < z < 0.4$	0.255	0.256	0.344
$0.4 < z < 0.5$	0.120	0.101	0.154
$0.5 < z < 0.6$	0.089	0.094	0.153
$0.6 < z < 0.7$	0.509	0.504	0.566
$0.7 < z < 0.8$	**2.753**	**2.604**	**1.932**
$0.8 < z < 0.9$	**2.657**	**2.473**	**1.947**
$0.9 < z < 1.0$	**1.136**	**1.137**	**0.944**
$1.0 < z < 1.1$	**0.489**	**0.440**	**0.394**
$1.1 < z < 1.2$	0.191	0.195	0.164
$1.2 < z < 1.3$	0.093	0.085	0.071
$1.3 < z < 1.4$	0.036	0.041	0.026
$1.4 < z < 1.5$	0.023	0.019	0.011
$1.5 < z < 10.0$	0.000	0.000	0.000

Table 6. Predicted σ_{D_V}/D_V, the 68 per cent confidence level error on the BAO distance D_V, based on the $n(z)$ of Table 5. For the SGC, we split the sample between the plates observed with $57656 \leq$ MJD ≤ 57711 (longer exposure times), and the plates observed with $57712 \leq$ MJD ≤ 57749 (nominal, shorter exposure times). The assumed areas are 620 deg^2 for the SGC and 600 deg^2 for the NGC. The last line displays the forecast at the effective redshift.

Redshift	SGC longer	SGC nominal	NGC	NGC and SGC nominal
$0.6 < z < 0.7$	0.162	0.163	0.153	0.112
$0.7 < z < 0.8$	0.059	0.060	0.069	0.045
$0.8 < z < 0.9$	0.053	0.054	0.060	0.040
$0.9 < z < 1.0$	0.071	0.071	0.079	0.053
$1.0 < z < 1.1$	0.112	0.121	0.135	0.090
$1.1 < z < 1.2$	0.224	0.221	0.259	0.168
$z_{\rm eff} = 0.84$	0.030	0.031	0.035	0.023

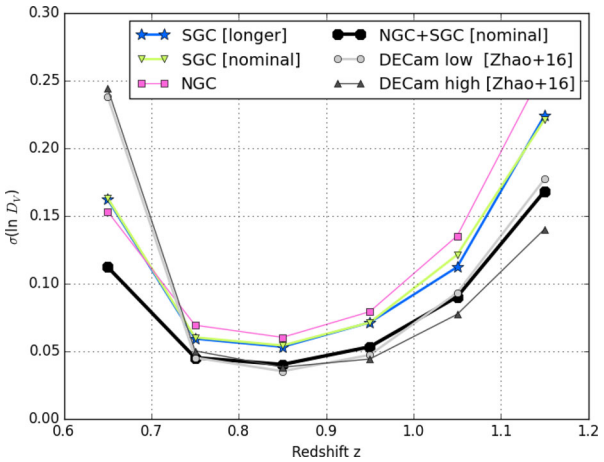

Figure 12. Predicted σ_{D_V}/D_V, the 68 per cent confidence level error of the BAO distance D_V, based on the $n(z)$ of Table 5. For the comparison, we report the values predicted in Zhao et al. (2016) for the two ELG selections used in that paper, DECam low and DECam high.

forecast of the eBOSS programme using the Fisher matrix formalism, including the expected precision on the BAO measurement with the ELG sample. In Zhao et al. (2016), three ELG selections were tested, amongst which two are close to our selection. We compare the original eBOSS ELG predictions to the prediction obtained from the number densities found in the final ELG programme and described in Table 5.

Except for the $n(z)$ and the areas, the forecast is performed using exactly the same methods and assumptions as in Zhao et al. (2016): the *Planck* cosmology (Planck Collaboration XIII 2016), a bias of $b(z) = 1.0G(0)/G(z)$, where $G(z)$ is the linear growth factor at redshift z ($b(z_{\rm eff}) \sim 1.5$ at the effective redshift $z_{\rm eff} = 0.84$, $z_{\rm eff}$ being the pair-weighted average redshift of the sample), an assumption of 50 per cent sample reconstruction. We present in Table 6 and Fig. 12 the predicted precision of the BAO distance D_V. The quantity D_V, defined as $D_V = [d_A^2(z)czH^{-1}(z)]^{1/3}$, is a combination of the angular diameter distance $d_A(z)$ and the Hubble parameter $H(z)$. It is the best-constrained distance with the BAO probe for an isotropic distribution of pairs, as it is composed of two transverse dimensions ($d_A^2(z)$) and one line-of-sight dimension ($czH^{-1}(z)$) (Eisenstein et al. 2005).

First, we observe that the predicted σ_{D_V}/D_V is very similar for the two SGC cases (longer and nominal), and these differ little from the prediction for the NGC. Fig. 12 shows that the predicted σ_{D_V}/D_V for the combined SGC+NGC sample is in broad agreement with the values predicted in Zhao et al. (2016) for the two then tested ELG selections (DECam low over 1400 deg^2 and DECam high over 1100 deg^2). The forecasts at the effective redshift confirm this: in Zhao et al. (2016), both ELG DECam selections provided a constraint of $\sigma_{D_V}/D_V = 0.022$ at the effective redshift; for the values reported in this paper, the forecast is $\sigma_{D_V}/D_V = 0.023$ at the effective redshift for the combined SGC and NGC samples. In addition, there is an improvement on the precision of BAO distance in the $0.6 < z < 0.7$ redshift bin.

5.6 Comparison with the ELG selection of Raichoor et al. (2016)

In this section, we compare the global properties of the final, DECam-based ELG target selection to the SDSS-based selection presented in Raichoor et al. (2016). The current selection has a higher average redshift (∼0.85 versus ∼0.75), a higher density (200–240 deg^{-2} versus 180 deg^{-2}), a slightly lower efficiency (∼65 per cent versus ∼70 per cent) and similar dependences to systematics. As explained in Dawson et al. (2016), the higher redshift of the current DECam-based ELG selection motivates our choice to use it for the eBOSS programme, as it allows eBOSS to measure the BAO scale at a redshift significantly higher than the LRGs ($z \sim 0.7$).

6 MEAN PROPERTIES OF THE ELGS OBSERVED IN THE SGC

In this section, we characterize the spectral properties, the structural properties and the stellar mass of the observed ELGs in the SGC. This analysis is based on the first months of observations ($57656 \leq$ MJD ≤ 57787), i.e. on ∼43 000 observed ELGs, amongst which ∼30 000 have a reliable $z_{\rm spec}$ estimation with $0.7 < z_{\rm spec} < 1.1$. This sample is already large enough to properly characterize the average properties of our ELGs.

6.1 Spectral properties from stacked spectra

The spectral properties are studied through stacked spectra, in order to maximize the signal-to-noise ratio of the typical features. Indeed, the average signal-to-noise ratio per pixel in the continuum region of the individual ELG spectra is low (see fig. 3 of Raichoor et al. 2016). The stacking is done as follows: the spectra are shifted to the rest frame and then median-stacked. We display in Fig. 13 the stacked spectrum obtained using all the ELGs with a reliable $0.7 < z_{\rm spec} < 1.1$ (top panel) and when stacking by redshift bins, g-band magnitude bins, and [O II] flux bins (bottom panels).

The full stacked spectrum (top panel) nicely displays the features typical from star-forming galaxies (e.g. Kennicutt 1992; Moustakas & Kennicutt 2006). For instance, the [O II] and [O III] emission lines clearly stand out, while weaker emission lines are also visible (e.g. [Ne III], Fe II*); the hydrogen Balmer recombination emission lines on top of relatively weak stellar Balmer absorption can be identified as well. Those are detailed in Zhu et al. (2015), which presents a similar stacked spectrum, though at a lower signal-to-noise ratio, as built from three times less individual spectra. When looking at the bottom panels, on the one hand, the spectra stacked by redshift bins are similar between them – the only difference being that the median flux is slightly decreasing with increasing redshift – indicating that we select ELGs with similar properties through the $0.7 < z_{\rm spec} < 1.1$ range. The same conclusion holds when stacking by g-band magnitude bins. On the other hand, when stacking by [O II] flux bins, we see differences in the shape of the spectra, as expected: the stellar absorption features around the 4000 Å break are stronger and the near-ultraviolet flux is weaker for low [O II] emitters.

6.2 Structural properties from the CS82 imaging

We here take advantage of the CFHT/MegaCam Stripe 82 Survey (CS82; PI: J.-P. Kneib; Erben et al., in preparation), which is an i-band imaging survey overlapping our ELG SGC footprint (see Fig. 9). The rest-frame wavelength probed by the i band at redshift 0.7 (0.8, 0.9 and 1.1, respectively) is ∼4400 Å(∼4150, ∼3950 and ∼3600 Å, respectively; see Fig. 13). CS82 covers ∼170 deg^2 down to $i \sim 24.0$ mag (5σ limiting magnitude in a 2 arcsec diameter aperture); its depth and excellent seeing (median value of 0.6 arcsec) makes this data set ideal to properly estimate the structural properties of the ELGs. There are ∼5000 observed ELGs with a reliable $0.7 < z_{\rm spec} < 1.1$ covered by CS82. We use images processed in a similar fashion to the CFHTLenS data set (Erben et al. 2013).

For each ELG, we cut out a 40 arcsec × 40 arcsec stamp image, masked neighbouring objects and used the GALFIT software (v3.0.5, Peng et al. 2010) to fit the surface brightness distribution with a Sersic (1968) profile $I(r) = I_e \times \exp\{-\kappa[(r/r_e)^{1/n_{\rm ser}} - 1]\}$, where $I(r)$ is the surface brightness at r, and I_e is the surface brightness at the effective radius r_e, which is the radius that encloses half of the emitted light. The Sérsic index $n_{\rm ser}$ translates the shape of the profile, with a higher value corresponding to a profile more peaked at the centre and with larger wings: $n_{\rm ser} = 4$ corresponds to a de Vaucouleurs (1948) profile, which is typical of early-type galaxies, while $n_{\rm ser} = 1$ corresponds to an exponential profile, typical of late-type galaxies. Wuyts et al. (2011) have shown that, for $0.1 < z_{\rm spec} < 2.5$, typical passive galaxies have $n_{\rm ser} \sim 4$, while typical star-forming galaxies have $n_{\rm ser} \sim 1$–2.

The initial parameter values (position, magnitude, size axial ratio, position angle) are set to the SEXTRACTOR (Bertin & Arnouts 1996) measurements. The sky is fixed during the fit, to the median value of the (masked) stamp. For each CFHT pointing, we use ∼50 bright, unsaturated ($18 \leq i_{\rm AB} \leq 21$) SDSS spectroscopic stars (Alam et al. 2015) to create a PSF stamp. The DECaLS pipeline also provides some size estimation, with fitting an $n_{\rm ser} = 1$ and an $n_{\rm ser} = 4$ profile. When restricting to objects classified as exponential by DECaLS and with $|n_{\rm ser} - 1| < 0.3$ in our measurements, the estimated sizes are in agreement (median of 0.01 arcsec for ∼1000 objects); there are not enough objects classified as de Vaucouleurs by DECaLS and with $|n_{\rm ser} - 4| < 0.3$ in our measurements to do a proper comparison (<20 objects).

6.3 Stellar masses

Additionally, we take advantage of the availability of near-infrared photometry in the DECaLS catalogues to estimate the stellar mass of the ELGs. The DECaLS pipeline also processes the *Wide-field Infrared Survey Explorer* (*WISE*) data (Wright et al. 2010). *WISE* – and its extension *NEOWISE* (Mainzer et al. 2011) – is an all-sky survey in four bands centred at 3.4, 4.6, 12 and 22 μm (*W*1, *W*2, *W*3 and *W*4). The DECaLS team re-processed the *WISE* images (Meisner, Lang & Schlegel 2017) and used them to do forced-photometry (Lang, Hogg & Schlegel 2016): the profiles corresponding to the sources detected in the DECam imaging are convolved

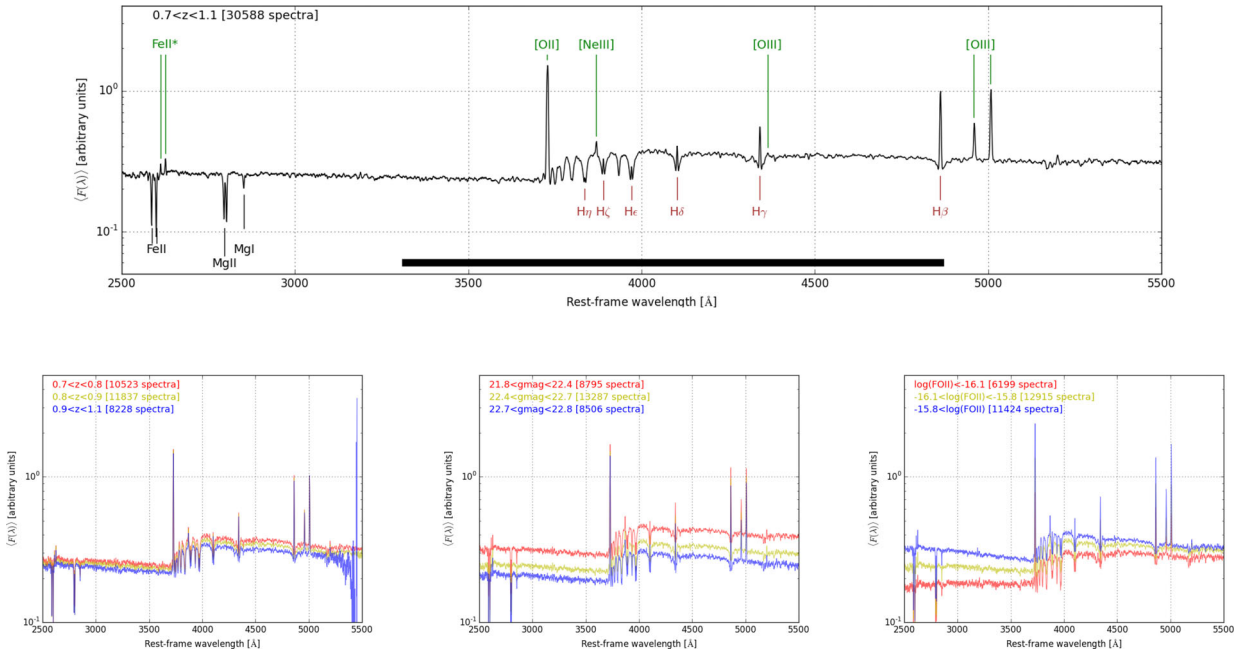

Figure 13. Median-stacked spectra, built from the currently 51 ELG plates observed in the SGC. *Top panel*: stacked spectrum obtained using all the ELGs with a reliable $z_{\rm spec}$ within $0.7 < z_{\rm spec} < 1.1$; the thick black line shows the rest-frame wavelength probed by the CS82 *i* band at $0.7 < z_{\rm spec} < 1.1$. We follow the colour-coding labelling of Zhu et al. (2015), with labelling emission features in green, interstellar/circumgalactic medium absorption lines in black and hydrogen Balmer lines with Greek symbols in brown. *Bottom panels*: stacked spectra from the same sample, when binning by $z_{\rm spec}$ (*left*), *g*-band magnitude (*middle*) and $\log_{10}(F_{[O\ II]})$ (*right*).

with the *WISE* PSF and the flux is fitted to the *WISE* imaging. This results in accurate colour measurements, with accounting for the PSF difference (∼1.5 arcsec for DECam and ∼6 arcsec for *WISE*).

We build the spectral energy distribution of the ELGs from the DECam/*grz* and *WISE*/*W*1*W*2 bands, and fit it with the FAST code (Kriek et al. 2009). We use the default settings: Bruzual & Charlot (2003) stellar population models with solar metallicity and a Chabrier (2003) initial mass function (IMF) to build delayed exponentially declining star formation history models ($SFR(t) \propto t \times e^{-t/\tau}$, with $8.5 < \log_{10}(\tau/Gyr) < 10$). During the fit, the redshift is fixed at $z_{\rm spec}$ and dust is allowed to follow the Kriek & Conroy (2013) law. The model is fitted to the data through a χ^2 minimization.

To validate our stellar mass estimate, we use the COSMOS2015 catalogue (Laigle et al. 2016). Laigle et al. (2016) use extremely accurate photometric redshifts and very deep optical and near-infrared imaging in more than 30 bands to estimate the stellar masses with Bruzual & Charlot (2003) models with a Chabrier (2003) IMF, resulting in very well constrained stellar masses. We select the ∼500 galaxies passing our ELG/SGC cuts in the ∼2 deg^2 of the COSMOS field, fix the redshift to the photometric redshift, and apply our fitting procedure. For the ∼300 galaxies with $0.7 < z_{\rm phot} < 1.1$, we find a difference of 0.05±0.21 dex between our stellar masses and those from Laigle et al. (2016), showing good agreement, given that the photometry is different and the settings are not exactly similar.

6.4 Properties overview

We present an overview of the properties of our ELG sample: photometric, spectroscopic, structural properties and stellar masses. We only consider here galaxies with a reliable $z_{\rm spec}$ within $0.7 < z_{\rm spec} < 1.1$ and covered by the CS82 imaging. The matrix plot in Fig. 14 compares the following quantities: $z_{\rm spec}$, $\log_{10}(F_{[O\ II]})$, *g*-band magnitude, $r - z$, $g - r$ and $r - W1$ colours, the stellar mass $\log_{10}(M_\star)$, the CS82 *i*-band magnitude, r_e, and $n_{\rm ser}$. As the $\log_{10}(F_{[O\ II]})$ is a key quantity for our ELG sample, we also split the data in bins of [O II]. We comment below only some of the information that can be read in this plot. Additionally, we provide in Table 7 the median and standard deviation for those quantities; we also provide those numbers when splitting this sample by bins of $z_{\rm spec}$, *g*-band magnitude, and $\log_{10}(F$[O II]).

As already presented above (Fig. 4), the $r - z$ and $g - r$ colours are correlated with $z_{\rm spec}$ and $\log_{10}(F_{[O\ II]})$: this motivated the use of the *grz* diagram for the ELG selection. By construction, as our sample is selected in *g* band, the *g*-band magnitude is not correlated with the $r - z$ and $g - r$ colours; however, a natural outcome of this construction is that the *i*-band magnitude is correlated with these colours: ELGs blue in $r - z$ or $g - r$ colours are faint in the *i* band. As a consequence, the *i*-band magnitude is anticorrelated with $\log_{10}(F_{[O\ II]})$. Regarding the structural parameters, our ELGs have on average sizes $r_e = 5.6 \pm 1.9$ and $n_{\rm ser} = 0.7 \pm 1.0$. The measured Sérsic indexes are typical for star-forming galaxies. We also note a strong correlation between the *i*-band magnitude and the size r_e (fainter objects are smaller). We also see a trend that strong [O II] emitters have a smaller $n_{\rm ser}$; however, it is difficult to exclude that this is not a consequence of the aforementioned correlations. The stellar mass displays some tight correlations with the $r - z$ and $r - W1$ colours. More massive galaxies will tend to be older, thus having a redder $r - z$ colour, which brackets the 4000 Å break; they will also tend to form less stars, as can be seen from the mild correlation between stellar mass and [O II] flux. The tight correlation with the $r - W1$ colour is expected, as the *WISE W*1 filter probes the rest-frame *H* band, dominated by emission from the low-mass stars constituting the bulk of a galaxy stellar mass.

To summarize from the [O II] emission point of view, in our ELG sample, the strong [O II] emitters have on average a slightly higher

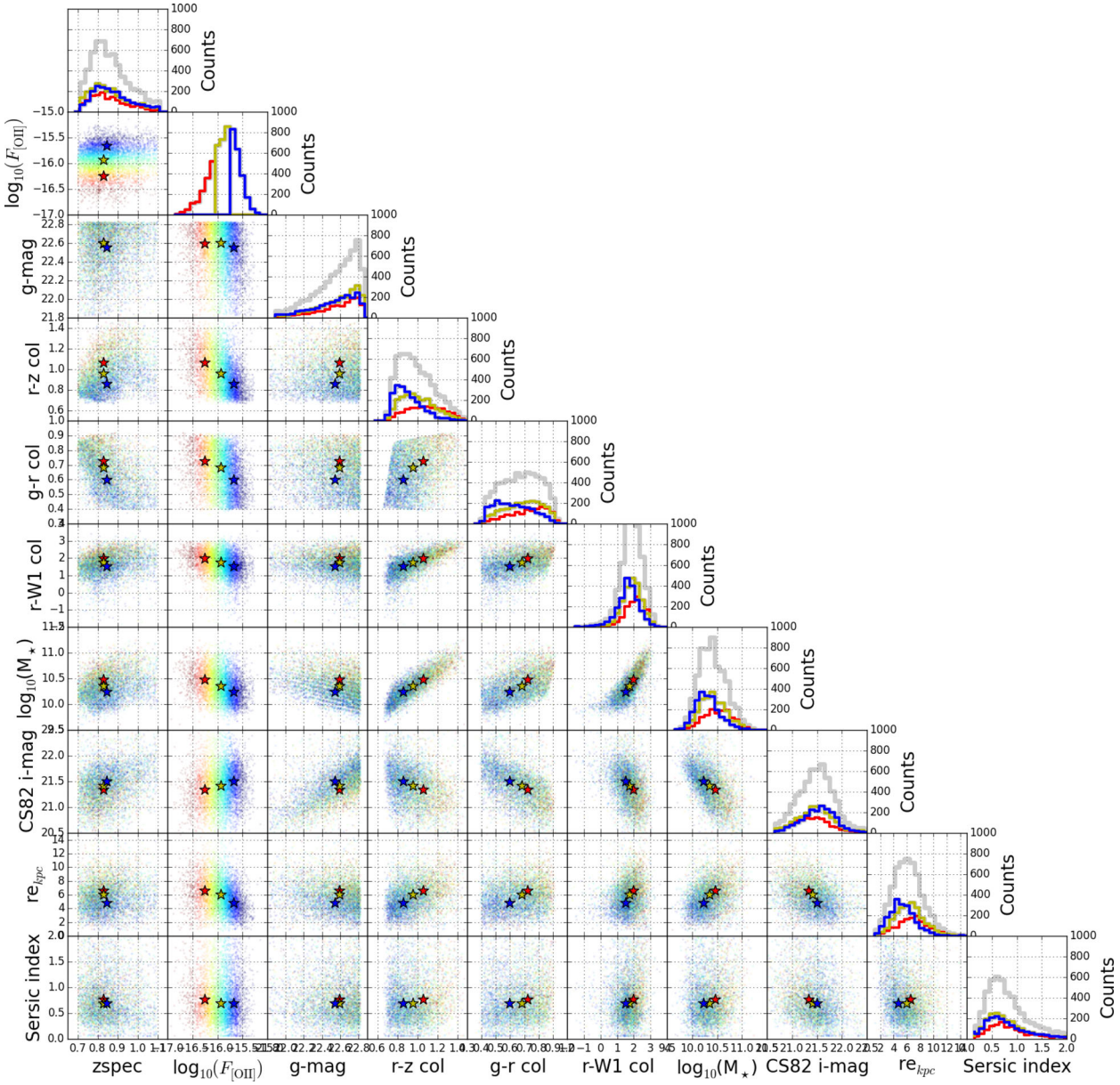

Figure 14. Matrix plot comparing the various properties of our ELG SGC sample, using objects covered by CS82, with a reliable $z_{\rm spec}$ and $0.7 < z_{\rm spec} < 1.1$ cover (∼5000 objects). We plot the histogram for this sample (grey), and when splitting it by [O II] flux bins [red: $log_{10}(F_{[O\ II]}) < -16.1$, yellow: $-16.1 < log_{10}(F_{[O\ II]}) < -15.8$ and blue: $log_{10}(F_{[O\ II]}) > -15.8$]. The red, yellow and blue stars in the scatter plots represent the median values for those bins in [O II] flux. In the scatter plots, the individual $log_{10}(F_{[O\ II]})$ is colour-coded, with a colour scale going from −16.5 (red) to −15.5 (blue).

$z_{\rm spec}$, bluer $r-z$ and $g-r$ colours, smaller stellar masses $\log_{10}(M_\star)$, fainter i-band magnitudes, smaller sizes, and slightly lower $n_{\rm ser}$.

7 CONCLUSION

We have presented the final target selection and first observations of the eBOSS/ELG programme. This programme will observe ∼255 000 ELGs over ∼1220 deg^2 with the goal of measuring the BAO scale at $z \sim 0.85$ with a ∼2 per cent precision. 300 plates are dedicated to this programme, split between the SGC and the NGC, the observation of which will last 2 yr. Observations started in 2016 September, with 51 plates observed in the SGC and 8 plates in the NGC ($57656 \leq \texttt{MJD} \leq 57787$) to date.

According to previous experience with BOSS and cosmological forecast, the target selection should fulfil the following criteria: (1) a surface density >170 deg^{-2}; (2) an absolute variation in expected density <15 per cent with respect to imaging depth, Galactic extinction and stellar density; (3) an absolute variation in expected density <15 per cent with respect to the estimated uncertainties in the imaging zero-point; (4) reliable $z_{\rm spec}$ measurements, i.e. with a precision better than 300 km s^{-1}; (5) an ELG sample used for cosmology at $z \sim 0.85$ >190 000, i.e. >74 per cent of the observed targets with a reliable $z_{\rm spec}$ measurement with $0.7 < z_{\rm spec} < 1.1$; (6) <1 per cent of this sample with a catastrophic $z_{\rm spec}$ measurement (redshift error exceeding 1000 km s^{-1}).

The ELG target selection is based on the DECaLS *grz*-band imaging, requiring clean photometry, favouring [O II] emitters through

Table 7. Mean properties for the ELG SGC sample. All samples are subsamples from the sample which will be used for cosmology (i.e. $0.7 < z_{\rm spec} < 1.1$ with a reliable $z_{\rm spec}$ measurement) overlapping the CS82 imaging survey. We report the median values and the standard deviation.

Sample	N	$z_{\rm spec}$	$\log_{10}(F[\mathrm{O\,II}])$ $[\log_{10}(\mathrm{erg\,s^{-1}\,cm^{-2}})]$	g mag (mag)	$g-r$ (mag)	$r-z$ (mag)	$r-W1$ (mag)	$\log_{10}(M_\star)$ $[\log_{10}(\mathrm{M}_\odot)]$	CS82 i mag (mag)	$r_{\rm e}$ (kpc)	$n_{\rm sersic}$
All	5235	0.83 ± 0.09	−15.88 ± 0.27	22.58 ± 0.23	0.66 ± 0.13	0.94 ± 0.17	1.69 ± 0.66	10.33 ± 0.26	21.44 ± 0.38	5.56 ± 1.93	0.71 ± 1.03
$0.7 < z_{\rm spec} < 0.8$	1816	0.76 ± 0.03	−15.91 ± 0.26	22.55 ± 0.25	0.74 ± 0.11	0.86 ± 0.13	1.55 ± 0.59	10.26 ± 0.22	21.34 ± 0.36	5.34 ± 1.81	0.74 ± 0.98
$0.8 < z_{\rm spec} < 0.9$	2053	0.84 ± 0.03	−15.88 ± 0.28	22.58 ± 0.23	0.64 ± 0.13	0.95 ± 0.17	1.72 ± 0.68	10.33 ± 0.26	21.43 ± 0.37	5.61 ± 1.93	0.69 ± 0.93
$0.9 < z_{\rm spec} < 1.1$	1366	0.97 ± 0.05	−15.85 ± 0.28	22.61 ± 0.22	0.57 ± 0.12	1.04 ± 0.18	1.93 ± 0.65	10.45 ± 0.27	21.60 ± 0.39	5.81 ± 2.05	0.70 ± 1.22
$21.825 < g-\mathrm{mag} < 22.4$	1404	0.82 ± 0.09	−15.84 ± 0.29	22.23 ± 0.15	0.68 ± 0.13	0.92 ± 0.17	1.75 ± 0.60	10.45 ± 0.25	21.10 ± 0.37	5.96 ± 1.97	0.76 ± 1.23
$22.4 < g-\mathrm{mag} < 22.7$	2320	0.84 ± 0.09	−15.88 ± 0.27	22.57 ± 0.09	0.66 ± 0.13	0.93 ± 0.17	1.67 ± 0.66	10.31 ± 0.25	21.45 ± 0.33	5.51 ± 1.91	0.70 ± 0.95
$22.7 < g-\mathrm{mag} < 22.825$	1511	0.84 ± 0.10	−15.92 ± 0.26	22.77 ± 0.04	0.65 ± 0.13	0.94 ± 0.18	1.66 ± 0.70	10.23 ± 0.25	21.63 ± 0.30	5.29 ± 1.86	0.69 ± 0.94
$log_{10}(F_{[O\,II]}) < -16.1$	1222	0.82 ± 0.09	−16.24 ± 0.17	22.60 ± 0.22	0.73 ± 0.13	1.06 ± 0.18	1.98 ± 0.60	10.46 ± 0.26	21.36 ± 0.40	6.31 ± 1.95	0.76 ± 1.12
$-16.1 < log_{10}(F_{[O\,II]}) < -15.8$	2045	0.83 ± 0.09	−15.93 ± 0.09	22.60 ± 0.23	0.69 ± 0.13	0.96 ± 0.17	1.74 ± 0.63	10.35 ± 0.25	21.42 ± 0.38	5.91 ± 1.86	0.69 ± 0.96
$-15.8 < log_{10}(F_{[O\,II]})$	1968	0.84 ± 0.09	−15.67 ± 0.12	22.55 ± 0.24	0.60 ± 0.13	0.86 ± 0.14	1.52 ± 0.67	10.24 ± 0.24	21.50 ± 0.37	4.73 ± 1.76	0.70 ± 1.05

a cut in the g-band magnitude and selecting galaxies in the desired redshift range, through a box cut in the *grz* space. The ELG footprint is split in two parts, one of 620 deg^2 over the SGC and one of 600 deg^2 over the NGC. To take advantage of the deeper DES observations over the SGC, the *grz* selection box is larger for the SGC, resulting in a target density higher than in the NGC (240 deg^{-2} versus 200 deg^{-2}).

We led a thorough analysis on the density variation over the footprint, similar to that presented in Delubac et al. (2017), and demonstrated that the ELG target selection passes the requirements on the target density variations. We use dedicated $z_{\rm spec}$ reliability flags (zQ, zCont): visual inspections on two plates reduced with the latest pipeline version show that those flags secure a catastrophic failure rate of 1.4 per cent ± 0.5 per cent. Results from the 51 plates already observed in the SGC provide a median $z_{\rm spec}$ of 0.84 and an efficiency of 68.0 per cent to 71.9 per cent. Results from the 8 plates already observed in the NGC provide a median $z_{\rm spec}$ of 0.84 and an efficiency of 63.1 per cent. Overall, the target selection reasonably passes all the requirements, though the efficiency is slightly lower than expected. The efficiency can be increased by including the $0.6 < z_{\rm spec} < 0.7$ redshift bin in the cosmological sample and by pipeline improvements. The cosmological forecast based on those first months measurements provide $\sigma_{D_V}/D_V = 0.023$, in agreement with the forecast in Zhao et al. (2016), which were performed before the start of the ELG observations.

Lastly, thanks to the current spectroscopic observations, completed with SED fitting using additional near-infrared photometry from the *WISE* satellite and with excellent seeing imaging coverage from the CS82 survey, we have presented a detailed view of the average properties (photometric, spectroscopic, structural properties and stellar masses) of the ELG sample in the SGC. The typical ELG in the SGC has a stellar mass of $\log(M_\star/\mathrm{M}_\odot) = 10.33 \pm 0.26$, a size of $r_e = 5.6 \pm 1.9$ kpc and a Sérsic index of $n_{\rm ser} = 0.7 \pm 1.0$. These present the typical features of star-forming galaxies, as seen in a composite spectrum stacking ∼30 000 ELG spectra, or with the 2D luminosity profile (low Sérsic index). These observations will be useful in the production of realistic mocks necessary for the cosmological analysis, and also illustrate the legacy of such a sample for the galaxy evolution studies. For instance, planned future work includes fitting the stacked spectra with stellar population models, in order to estimate precisely the average properties of those ELGs, including mass, age and star formation history.

The target catalogue over the SGC footprint will be publicly released in mid-2017, as a Value-Added Catalog from the SDSS DR14 release (http://www.sdss.org/dr14/data_access/vac/).

This ELG selection is paving the way for the future large BAO surveys, such as DESI and 4MOST, in which ELGs will constitute a significant part of the targets.

ACKNOWLEDGEMENTS

Author contributions: AR, TD and JPK acknowledge support from the ERC advanced grant LIDA. WJP acknowledges support from the European Research Council through the Darksurvey grant 614030, and from the UK Science and Technology Facilities Council grant ST/N000668/1 and UK Space Agency grant ST/N00180X/1. EJ acknowledges support from the OCEVU Labex (ANR-11-LABX-0060).

This paper represents an effort by both the SDSS-IV collaborations. Funding for SDSS-III was provided by the Alfred P. Sloan Foundation, the Participating Institutions, the National Science Foundation and the U.S. Department of Energy Office of

Science. Funding for the Sloan Digital Sky Survey IV has been provided by the Alfred P. Sloan Foundation, the U.S. Department of Energy Office of Science and the Participating Institutions. SDSS-IV acknowledges support and resources from the Center for High-Performance Computing at the University of Utah. The SDSS web site is www.sdss.org. SDSS-IV is managed by the Astrophysical Research Consortium for the Participating Institutions of the SDSS Collaboration including the Brazilian Participation Group, the Carnegie Institution for Science, Carnegie Mellon University, the Chilean Participation Group, the French Participation Group, Harvard-Smithsonian Center for Astrophysics, Instituto de Astrofísica de Canarias, the Johns Hopkins University, Kavli Institute for the Physics and Mathematics of the Universe (IPMU)/University of Tokyo, Lawrence Berkeley National Laboratory, Leibniz Institut für Astrophysik Potsdam (AIP), Max-Planck-Institut für Astronomie (MPIA Heidelberg), Max-Planck-Institut für Astrophysik (MPA Garching), Max-Planck-Institut für Extraterrestrische Physik (MPE), National Astronomical Observatory of China, New Mexico State University, New York University, University of Notre Dame, Observatário Nacional/MCTI, The Ohio State University, Pennsylvania State University, Shanghai Astronomical Observatory, United Kingdom Participation Group, Universidad Nacional Autónoma de México, University of Arizona, University of Colorado Boulder, University of Portsmouth, University of Utah, University of Virginia, University of Washington, University of Wisconsin, Vanderbilt University and Yale University.

This paper presents observations obtained at Cerro Tololo Inter-American Observatory, National Optical Astronomy Observatory (NOAO Prop. ID: 2014B-0404; co-PIs: D. J. Schlegel and A. Dey), which is operated by the Association of Universities for Research in Astronomy (AURA) under a cooperative agreement with the National Science Foundation. This paper also includes DECam observations obtained as part of other projects, namely the Dark Energy Survey (DES, NOAO Prop. ID: 2012B-0001).

DECaLS used data obtained with the Dark Energy Camera (DECam), which was constructed by the Dark Energy Survey (DES) collaboration. Funding for the DES Projects has been provided by the U.S. Department of Energy, the U.S. National Science Foundation, the Ministry of Science and Education of Spain, the Science and Technology Facilities Council of the United Kingdom, the Higher Education Funding Council for England, the National Center for Supercomputing Applications at the University of Illinois at Urbana-Champaign, the Kavli Institute of Cosmological Physics at the University of Chicago, Center for Cosmology and Astro-Particle Physics at the Ohio State University, the Mitchell Institute for Fundamental Physics and Astronomy at Texas A&M University, Financiadora de Estudos e Projetos, Fundação Carlos Chagas Filho de Amparo, Financiadora de Estudos e Projetos, Fundação Carlos Chagas Filho de Amparo à Pesquisa do Estado do Rio de Janeiro, Conselho Nacional de Desenvolvimento Científico e Tecnológico and the Ministério da Ciência, Tecnologia e Inovacão, the Deutsche Forschungsgemeinschaft and the Collaborating Institutions in the Dark Energy Survey. The Collaborating Institutions are Argonne National Laboratory, the University of California at Santa Cruz, the University of Cambridge, Centro de Investigaciones Enérgeticas, Medioambientales y Tecnológicas-Madrid, the University of Chicago, University College London, the DES-Brazil Consortium, the University of Edinburgh, the Eidgenössische Technische Hochschule (ETH) Zürich, Fermi National Accelerator Laboratory, the University of Illinois at Urbana-Champaign, the Institut de Ciències de l'Espai (IEEC/CSIC), the Institut de Física d'Altes Energies, Lawrence Berkeley National Laboratory, the Ludwig-Maximilians Universität München and the associated Excellence Cluster Universe, the University of Michigan, the National Optical Astronomy Observatory, the University of Nottingham, the Ohio State University, the University of Pennsylvania, the University of Portsmouth, SLAC National Accelerator Laboratory, Stanford University, the University of Sussex and Texas A&M University.

This publication uses data products from the *Wide-field Infrared Survey Explorer*, which is a joint project of the University of California, Los Angeles, and the Jet Propulsion Laboratory/California Institute of Technology, and *NEOWISE*, which is a project of the Jet Propulsion Laboratory/California Institute of Technology. *WISE* and *NEOWISE* are funded by the National Aeronautics and Space Administration.

Author contributions AR led this paper, designed the target selection, analysed the ELG plates and estimated the structural properties and stellar masses. JC led the $z_{\rm spec}$ measurement, developed the $z_{\rm spec}$ confidence flag, the spectra stacking procedure, and installed and ran the DECaLS pipeline on the Utah machines (with JRB). TD led the systematics analysis. JPK, ChY, KSD and WJP supervised the ELG programme. JC, TD, KSD and CG did the visual inspection. AJR, YW and GBZ did the cosmological forecast. HJS and JLT led the tiling, VM led the spectroscopic observations, JB and JRB led the spectroscopic pipeline reduction. AD, DL and DJS led the DECaLS imaging observation and pipeline development. JM and NPD reviewed the ELG programme and participated in the ELG programme development. EJ, JAN, FP and GBZ also participated in the ELG programme development.

REFERENCES

Abazajian K. N. et al., 2009, ApJS, 182, 543
Abolfathi B. et al., 2017, ApJS, preprint (arXiv:1707.09322)
Alam S. et al., 2015, ApJS, 219, 12
Bertin E., Arnouts S., 1996, A&AS, 117, 393
Blanton M. R. et al., 2017, AJ, 154, 28
Bolton A. S. et al., 2012, AJ, 144, 144
Bruzual G., Charlot S., 2003, MNRAS, 344, 1000
Chabrier G., 2003, PASP, 115, 763
Cole S. et al., 2005, MNRAS, 362, 505
Colless M. et al., 2003, preprint (arXiv:astro-ph/0306581)
Comparat J. et al., 2013, MNRAS, 428, 1498
Comparat J. et al., 2016a, A&A, 592, A121
Comparat J. et al., 2016b, MNRAS, 461, 1076
Coupon J. et al., 2009, A&A, 500, 981
de Jong R. S. et al., 2014, Proc. SPIE, 9147, 91470M
de Vaucouleurs G., 1948, Ann. Astrophys., 11, 247
Dawson K. S. et al., 2013, AJ, 145, 10
Dawson K. S. et al., 2016, AJ, 151, 44
Delubac T. et al., 2015, A&A, 574, A59
Delubac T. et al., 2017, MNRAS, 465, 1831
DESI Collaboration et al., 2016a, preprint (arXiv:1611.00036)
DESI Collaboration et al., 2016b, preprint (arXiv:1611.00037)
Drinkwater M. J. et al., 2010, MNRAS, 401, 1429
Eisenstein D. J. et al., 2001, AJ, 122, 2267
Eisenstein D. J. et al., 2005, ApJ, 633, 560
Eisenstein D. J. et al., 2011, AJ, 142, 72
Erben T. et al., 2013, MNRAS, 433, 2545
Finkbeiner D. P. et al., 2016, ApJ, 822, 66
Flaugher B. et al., 2015, AJ, 150, 150
Gunn J. E. et al., 2006, AJ, 131, 2332
Guzzo L. et al., 2014, A&A, 566, A108
Gwyn S. D. J., 2012, AJ, 143, 38
Hutchinson T. A. et al., 2016, AJ, 152, 205
Ilbert O. et al., 2006, A&A, 457, 841

Jensen T. W. et al., 2016, ApJ, 833, 199
Kaiser N. et al., 2010, Proc. SPIE, 7733, 77330E
Kennicutt R. C., Jr, 1992, ApJ, 388, 310
Kriek M., Conroy C., 2013, ApJ, 775, L16
Kriek M., van Dokkum P. G., Labbé I., Franx M., Illingworth G. D., Marchesini D., Quadri R. F., 2009, ApJ, 700, 221
Laigle C. et al., 2016, ApJS, 224, 24
Lang D., Hogg D. W., Schlegel D. J., 2016, AJ, 151, 36
Laureijs R. et al., 2011, preprint (arXiv:1110.3193)
Lilly S. J., Le Fevre O., Hammer F., Crampton D., 1996, ApJ, 460, L1
Madau P., Dickinson M., 2014, ARA&A, 52, 415
Madau P., Pozzetti L., Dickinson M., 1998, ApJ, 498, 106
Mainzer A. et al., 2011, ApJ, 731, 53
Meisner A. M., Lang D., Schlegel D. J., 2017, AJ, 153, 38
Morganson E. et al., 2015, ApJ, 806, 244
Moustakas J., Kennicutt R. C., Jr, 2006, ApJS, 164, 81
Moustakas J., Kennicutt R. C., Jr, Tremonti C. A., 2006, ApJ, 642, 775
Myers A. D. et al., 2015, ApJS, 221, 27
Oke J. B., Gunn J. E., 1983, ApJ, 266, 713
Palanque-Delabrouille N. et al., 2016, A&A, 587, A41
Peng C. Y., Ho L. C., Impey C. D., Rix H.-W., 2010, AJ, 139, 2097
Planck Collaboration XIII, 2016, A&A, 594, A13
Prakash A. et al., 2016, ApJS, 224, 34
Raichoor A. et al., 2016, A&A, 585, A50
Ross A. J. et al., 2011, MNRAS, 417, 1350
Ross A. J. et al., 2017, MNRAS, 464, 1168
Schlegel D. J., Finkbeiner D. P., Davis M., 1998, ApJ, 500, 525
Scodeggio M. et al., 2016, Astron. Astrophys., preprint (arXiv:1611.07048)
SDSS Collaboration et al., 2016, ApJS, preprint (arXiv:1608.02013)
Sersic J. L., 1968, Atlas de galaxias australes. Observatorio Astronomico, Cordoba, Argentina
Smee S. A. et al., 2013, AJ, 146, 32
Sugai H. et al., 2012, Proc. SPIE, 8446, 84460Y
Takada M. et al., 2014, PASJ, 66, R1
Wright E. L. et al., 2010, AJ, 140, 1868
Wuyts S. et al., 2011, ApJ, 742, 96
York D. G. et al., 2000, AJ, 120, 1579
Zhao G.-B. et al., 2016, MNRAS, 457, 2377
Zhu G. B. et al., 2015, ApJ, 815, 48

[1]*Institute of Physics, Laboratory of Astrophysics, Ecole Polytechnique Fédérale de Lausanne (EPFL), Observatoire de Sauverny, CH-1290 Versoix, Switzerland*
[2]*CEA, Centre de Saclay, IRFU/SPP, F-91191 Gif-sur-Yvette, France*
[3]*Departamento de Fisica Teorica, Universidad Autonoma de Madrid, Cantoblanco E-28049, Madrid, Spain*
[4]*Instituto de Física Teórica, (UAM/CSIC), Universidad Autónoma de Madrid, Cantoblanco, E-28049 Madrid, Spain*
[5]*Max-Planck-Institut für extraterrestrische Physik (MPE), Giessenbachstrasse 1, D-85748 Garching bei München, Germany*
[6]*Aix Marseille Université, CNRS, LAM (Laboratoire d'Astrophysique de Marseille), UMR 7326, F-13388 Marseille, France*
[7]*Lawrence Berkeley National Labortatory, 1 Cyclotron Rd, Berkeley, CA 94720, USA*
[8]*Department of Physics and Astronomy, University of Utah, Salt Lake City, UT 84112, USA*
[9]*Institute of Cosmology and Gravitation, Dennis Sciama Building, University of Portsmouth, Portsmouth PO1 3FX, UK*
[10]*National Optical Astronomy Observatory, Tucson, AZ 85719, USA*
[11]*Bruce and Astrid McWilliams Center for Cosmology, Department of Physics, Carnegie Mellon University, 5000 Forbes Ave, Pittsburgh, PA 15213, USA*
[12]*Department of Physics and Astronomy, Ohio University, 251B Clippinger Labs, Athens, OH 45701, USA*
[13]*Center for Cosmology and Particle Physics, Department of Physics, New York University, 4 Washington Place, New York, NY 10003, USA*
[14]*Center for Cosmology and Astro-Particle Physics, Ohio State University, Columbus, OH 43210, USA*
[15]*National Astronomy Observatories, Chinese Academy of Science, Beijing 100012, P. R. China*
[16]*Department of Physics and Astronomy, Siena College, 515 Loudon Road, Loudonville, NY 12211, USA*
[17]*Department of Physics and Astronomy and PITT PACC, University of Pittsburgh, Pittsburgh, PA 15260, USA*
[18]*Campus of International Excellence UAM+CSIC, Cantoblanco, E-28049 Madrid, Spain*
[19]*Instituto de Astrofísica de Andalucía (CSIC), Glorieta de la Astronomía, E-18080 Granada, Spain*
[20]*Center for Astrophysical Sciences, Department of Physics and Astronomy, Johns Hopkins University, 3400 North Charles Street, Baltimore, MD 21218, USA*

This paper has been typeset from a TEX/LATEX file prepared by the author.